Effect of forging on the low cycle fatigue behavior of cast AZ31B Alloy

D. Toscano, S.K. Shaha, B. Behravesh, H. Jahed, B. Williams

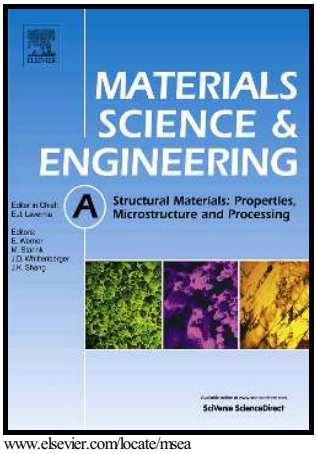

www.elsevier.com/locate/msea

PII: S0921-5093(17)31101-2
DOI: http://dx.doi.org/10.1016/j.msea.2017.08.086
Reference: MSA35434

To appear in: *Materials Science & Engineering A*

Received date: 26 May 2017
Revised date: 22 August 2017
Accepted date: 23 August 2017

Cite this article as: D. Toscano, S.K. Shaha, B. Behravesh, H. Jahed and B. Williams, Effect of forging on the low cycle fatigue behavior of cast AZ31B Alloy, *Materials Science & Engineering A,* http://dx.doi.org/10.1016/j.msea.2017.08.086

Effect of forging on the low cycle fatigue behavior of cast AZ31B Alloy

D. Toscano [a], S. K. Shaha[a], B. Behravesh[a], H. Jahed[1 a], B. Williams[b]

[a]Department of Mechanical & Mechatronics Engineering, University of Waterloo, 200 University Ave W, Waterloo, ON N2L 3G1, CANADA

[b]CanmetMATERIALS, Natural Resources Canada, 183 Longwood Road South, Hamilton, ON L8P 0A1, Canada

Abstract

The effect of forging on the low cycle fatigue (LCF) behavior of cast AZ31B was investigated. The forging process was conducted at a temperature of 450°C and speed of 390mm/min. Fully reversed (R_ε=-1) strain controlled cyclic tests were performed on as-cast and forged materials under total strain amplitudes of 0.1%-1.2%. Forging eliminated the dendritic morphology and reduced β-phase intermetallics observed in the cast alloy. Additionally sharp basal texture and bimodal grain structure were developed. Generally, the forged material was found to exhibit longer fatigue life, especially at lower strain amplitudes. This was attributed to the grain refinement and the developed basal texture that changed the alloy's deformation behavior. Also, the forged material achieved significantly higher stresses at the same total strain amplitudes compared to cast AZ31B, and substantial cyclic hardening occurred during cyclic loading. At the same time, considerable tension-compression asymmetry was observed in the forged AZ31B during LCF testing. The Smith-Watson-Topper model and Jahed-Varvani energy model were employed and both models were found to accurately predict the experimentally obtained fatigue life of both alloy conditions. The Jahed-Varvani model accurately predicted fatigue life within a factor of 1.5 especially for the asymmetric behavior of forged AZ31B.

Keywords: Low-cycle-fatigue; Forging; Texture; Microstructure; AZ31B-Magnesium; Modelling

1 Corresponding author: hjahed@uwaterloo.ca

1. Introduction

Corporate Average Fuel Economy (CAFE) regulations are requiring automotive manufacturers to achieve fleet-wide average fuel economy ratings of 54.5 miles/gallon by 2025 [1]. Such aggressive emission targets have led to manufacturers investing heavily in lightweighting technologies to reduce emissions by reducing vehicle weight [2]. Magnesium (Mg) alloys in particular have attracted much attention due to their high specific strength, good recyclability and excellent machinability [3, 4]. Additionally, Mg is the lightest structural metal having a density two-thirds that of aluminum, which allows for the fabrication of components weighing substantially less than components fabricated from aluminum or steel alloys [5]. Wrought Mg alloys also exhibit superior quasi-static [6] and cyclic [7] loading behavior compared to their cast alternatives. Therefore, wrought Mg alloys are attractive and viable candidates for load-bearing components.

Forging is a thermo-mechanical process used to produce wrought Mg alloys. During the forgings process, a pre-form of the material is deformed between two dies of a hydraulic press, often at elevated temperatures. The applied forging load results in severe plastic deformation of the material allowing it to take the desired shape. Forming at elevated temperatures results in the nucleation and growth of new grains in the material through *dynamic recrystallization*, resulting in grain refinement in the forged component compared to the pre-forged material [8, 9]. Studies conducted by Koike et al. [10], and Marya et al. [11] among others on AZ31 alloy have observed an improvement in material properties as grain size decreases attributable to increased impedance to dislocation motion due to higher grain boundary density. Consequently, the forging process is expected to increase the yield and ultimate strengths of the alloy due to grain refinement [12, 13]. This improvement in strength is then expected to increase the low cycle fatigue life of the material due to lower fatigue damage (i.e. plastic strain) occurring for a given applied stress/strain amplitude compared to a lower strength material. Such an improvement in fatigue life due to grain refinement via extrusion [14] and rolling [15] has also been previously noted.

Another microstructural impact of the forging process on Mg alloys is the development of a preferred unit cell orientation or "*texture*" inside the material due to the hexagonal close packed (HCP) crystal structure of Mg and its alloys [16, 17]. This developed texture is responsible for the well documented "twin" deformation and tension-compression asymmetry in wrought Mg alloys [18, 19]. During thermo-mechanical deformations, such as forging, the c-axis of the Mg unit cell re-orients itself to be parallel to the localized deformation direction [20]. This texture development in Mg alloys is thought to be due to the occurrence of rotational dynamic recrystallization caused by the activation of non-basal (prismatic <a>, pyramidal I <a> and pyramidal II <c+a>) slip systems [21, 22]. The tension-compression asymmetry resulting from the developed texture has been shown to affect the fatigue life of Mg alloys due to accumulation of fatigue damage due to $\{10\bar{1}2\}\langle 10\bar{1}1\rangle$ twins [15, 23], and also the development of a mean stress under fully reversed strain-controlled condition [24]. Such a developed mean stress could be either beneficial (mean compressive stress) or detrimental (mean tensile stress) to the overall fatigue resistance of the alloy.

To date, there are no comparative studies that investigate the effect of forging on the fatigue resistance of an as-received Mg alloy (as would for example, be implemented in a manufacturing environment). To the best of the authors' knowledge, the only available study concerning the fatigue examination of forged AZ31B was performed by Kang et al. [25]. This study compared the tensile strengths, load-controlled fatigue strengths, and hardness between forged AZ31B and cast AM60. The authors did not provide the details of the employed forging process and the study was limited to an evaluation of the alloys fatigue strength and microstructure. However, other studies investigating the fatigue behavior of wrought Mg alloys processed via alternative thermo-mechanical processes such as rolling and extrusion have been reported in literature. While not directly applicable to the proposed forging process, the results of these studies do shed some light on the effect of thermo-mechanical processing on the fatigue behavior of Mg alloys. Huppman et al. [26] examined strain- and stress-controlled uniaxial fatigue behavior of extruded AZ31 alloy with varying final microstructures and noted superior fatigue resistance of the finer grained condition owing to a suppression in twin activation and lower plastic strain during cycling. Similarly, Kamakura et al. [27] investigated the effect of extrusion temperature on the stress-controlled fatigue life of AZ31 Mg alloy and reported an improvement in fatigue life and

an increased fatigue limit (at 10^7 cycles) particularly for AZ31 alloy as grain size decreased. Park et al. [28] investigated the low-cycle behavior of rolled AZ31through both stress- and strain-controlled tests. The authors noted that the sharp basal texture in the wrought alloy resulted in asymmetric tension-compression deformation behavior during cyclic loading which resulted in the development of a tensile mean stress. A buildup of residual twins with continued cycling was also found to affect the cyclic hardening behavior of the alloy. Similar results were reported for rolled AZ31B by Wu et al. [29] who examined LCF behavior in the rolling- (RD), transverse- (TD) and normal (ND) directions. In their study, the authors noted similar fatigue behavior in the RD and TD due to in-plane texture symmetry. The authors' also noted the significant contribution of twinning/de-twinning behavior on the fatigue life of the alloy. Consequently, much work remains to be performed in order to characterize fully the fatigue behavior of forged AZ31B.

This paper aims to examine the effect of open-die forging on the microstructural and mechanical behavior (especially the LCF properties) of cast AZ31B alloy. A cast condition was selected as the starting material in this investigation, because casting is a widely used and cost-efficient method of producing pre-forms of relatively complex geometries, albeit with typically poorer mechanical properties than their wrought counterparts [30]. A strain-based and an energy-based fatigue model is employed to predict the fatigue life of the as-cast and forged AZ31B. Both of the models offer successful predictions within the tested strain amplitudes.

2. Experimental Details

2.1 Sample preparation

In this study, as-cast AZ31B (Table 1) was the starting material which was delivered by Magnesium-Elektron in a circular billet with a radius of 300 mm and a height of 500 mm (Fig. 1a). A cylindrical billet of the cast AZ31B with a diameter of 63.5 mm and a length of 65 mm was extracted from the larger as-cast billet for the forging process (Fig. 1b). Prior to forging, this billet was heated to a temperature of 450°C for 3 hours to ensure an even distribution of temperature throughout the billet (effectively homogenizing the cast material). The heated billet was then placed between isothermal flat dies of a hydraulic press such that the upsetting

direction lay along the radial direction of the billets (Fig. 1c). The forging was conducted in a single step up to a final compressive engineering strain of 80% with an initial ram speed of 390 mm/min. The final forging had approximate dimensions of 135 mm × 130 mm × 13 mm. The forged piece was air-cooled to room temperature.

Dog-bone shape specimens with a gauge length of 25 mm, width of 6 mm and thickness of 4 mm were extracted for tensile and fatigue tests following ASTM E8 (Fig. 1d). The as-cast specimens were extracted from locations such that the sample gauge lay at 0.75 of the as-received billet radius. These specimens were extracted in three directions: longitudinal direction (LD), radial direction (RD), and transverse direction (TD) to confirm the homogeneity of the as-cast material. The specimen geometry for forged material was the same as discussed above and were extracted such that the testing direction was aligned with LD of the forging (Fig. 1e). All specimen surfaces were ground with #2000 SiC paper to remove machining marks prior to testing.

2.2 Microstructure and texture analysis

A sample for the microstructural and texture study was extracted from a radial distance of 75 mm from the as-cast billet. For the forged material, microstructure and texture was examined at the edge, one-quarter and one-half the width of the forged coupon to investigate the effect of non-homogenous strain distribution during the forging process. Microstructure specimens were prepared by grinding with progressively finer SiC paper up to #1200. After grinding, specimens were polished with 6, 3, 1 and 0.1-μ diamond paste with oil based lubricant on imperial cloth followed by a final polishing with 0.05-μ master prep colloidal silica solution on a black CHEM pad. Polished samples were then etched with acetic-picral as outlined in Roostaei et al. [24]. Microstructures were investigated using a FEI Quanta Scanning Electron Microscope (SEM) equipped with a Field Emission Gun (FEG) and an Oxford Energy Dispersive X-ray (EDX) detector. For all observations, the SEM was operated at an accelerating voltage of 20 kV. The volume fraction of the secondary phases were calculated using *ImageJ* software.

The phase identification (PID) and crystallographic texture of the same polished samples was examined using a Bruker D8-Discover equipped with a VÅNTEC-500 area detector and using Cu-Kα radiation at 40kV and 40 mA. During the PID measurement, the scan was performed in θ/2θ mode from 20 to 90° with a step size of 15° and 60 sec/step, while the incident beam and the detector were placed at a fixed 2θ angle of 40° for texture measurement. The samples were

tilted between 0° and 75° with a step of 15° considered as the Ψ-scan while the sample rotation known as Φ-scan was between 0° and 360° with a step size of 5°. The sample was scanned for 20s at each orientation. The Debye–Scherrer diffraction rings were collected using the area detector in a two-dimensional diffraction image. Then, the incomplete pole figures for the $\{0001\}$, $\{10\bar{1}0\}$, $\{10\bar{1}1\}$ and $\{1\bar{1}02\}$ planes were extracted from the diffraction rings. The complete pole figures were then calculated using the DIFFRAC.Suite:Texture software while the phases were evaluated using DIFFRAC.EVA.

2.3 Strain controlled fatigue test

Fully reversed ($R_\varepsilon = -1$) strain controlled fatigue testing of both as-cast and forged material was performed on an MTS 810 servo hydraulic load frame equipped with a 25kN actuator and a MTS FlexTest 40 controller in accordance with ASTM E606. Strain was captured using a MTS extensometer with a gauge of 7.6 mm. The extensometer was mounted to the specimens using steel springs and secured with Loctite 380 instant adhesive as well as Loctite 7452 accelerant. Testing was performed at total strain amplitudes from 0.1% to 1.2% at increments of 0.1% and the test frequency was varied between 0.2 Hz and 2.5 Hz depending on the tested strain amplitude such that the average strain rate during testing was constant at 0.01 s^{-1}. A specimen was considered to have failed when the tensile load dropped to 50% of its peak value or the specimen fractured. For tests extending past 10^4 cycles, the test was paused when the peak tensile and compressive forces stabilized and the test was changed over to load control mode operating at a frequency of 30 Hz until failure or a cycle count of 10^7 cycles (considered as runout) was achieved. Fractured specimens were retained for fractographic analysis using the same SEM outlined above. Several fracture samples were polished and etched as outlined earlier in order to observe the microstructural changes during fatigue testing. These microstructures were investigated using an Olympus BX51M metallurgical microscope.

3. Results

3.1 Microstructure and texture prior to testing

Fig. 2a, b illustrates SEM micrographs of as-cast AZ31B Mg alloy obtained in backscatter imaging (BSE) mode. It is seen that the cast AZ31B alloy exhibits porosity (a typical casting defect), and a dendritic morphology with large equiaxed grains of average grain size 278 μm ± 30. At the same time, a network of intermetallics containing Al, Zn with Mg were identified using EDX point analysis (Fig. 2i–g) and x-ray diffraction phase analysis as seen in Fig. 2h. This indicated the presence of α-Mg and a eutectic phase containing β-$Mg_{17}Al_{12}$ and intermetallics of $MgZn_2$ particles formed in the inter-dendritic regions during solidification. Image analysis of as-cast micrographs indicated approximately 9.8% combined volume fraction for the β-phase and intermetallic particles. Similar particles were reported for other AZ Mg-alloys [31]. In contrast, the forged alloy exhibited bimodal morphology composed of large flattened grains surrounded by considerably finer recrystallized grains. The average size of these recrystallized grains was calculated to be 14 μm ± 5. BSE imaging indicated that forging eliminated the dendritic morphology and porosity in the alloy (Fig. 2c) while the $MgZn_2$ intermetallic were dissolved back into the matrix (Fig. 2d,g and h). A similar image analysis as described above indicated that forging reduced the intermetallic volume fraction to approximately 1.6% with only $Mg_{17}Al_{12}$ particles observed after forging.

Texture analysis of the as-cast alloy indicated that the c-axis of the HCP unit cells were randomly oriented in the material as expected in a cast product. Specifically, pole figures (PFs) for the basal (0002) and prismatic $(10\bar{1}0)$ planes respectively (Fig. 3a) indicated a maximum intensity of 4.57 and 4.62 MRD (Multiples of Random Distributions) suggesting that the cast material displayed low texture intensity with no preferential unit cell orientation (illustrated schematically in Fig. 3a). By contrast, the forged material exhibited a strong basal texture with a high texture intensity of 11.82 and 3.14 MRD for the PFs of (0002) and $(10\bar{1}0)$ planes, respectively. The obtained PFs for forged material indicated a set of basal $\{0001\}\langle 2\bar{1}\bar{1}0\rangle$ textures such that c-axis of the HCP unit cells were oriented more or less parallel to the forging direction (FD) as illustrated schematically in Fig. 3b.

3.2 Quasi-static stress-strain properties

The true stress-true strain plots of the AZ31B alloy in as-cast and forged conditions tested at room temperature is shown in Fig. 4 and the Yield Strength (YS), Ultimate Tensile Strength (UTS) and elongation are summarized in Table 2. It is observed that the forged alloy shows considerable improvement in the tensile YS and UTS, but lower ductility compared to the as-cast material. Another interesting feature is the exhibited tension and compression asymmetry especially in the forged material. The as-cast alloy displays slight sigmoidal behavior between 2 to 8 percent true strain (enclosed by the dotted ellipse) in both tension and compression suggesting the activation of $\{10\bar{1}2\}\langle 10\bar{1}1\rangle$ extension twin in certain favorably oriented grains [32, 33]. However, due to the random texture of the as-cast material, little anisotropy between LD, TD and RD and virtually no asymmetry in tension and compression was observed [34, 35]. In contrast, the forged material displayed significant tension-compression asymmetry in the LD and TD directions due to favourable unit-cell orientation for $\{10\bar{1}2\}\langle 10\bar{1}1\rangle$ twin activation in compression whereas compression along the FD did not show any sigmoidal behavior suggesting that the deformation was dominated by slip instead of twinning [36, 37]. Similarly, a lack of sigmoidal behavior in tension indicated slip dominated deformation for the forged condition. The substantial increase in the forged YS compared to the as-cast alloy is attributed both to grain refinement and unfavourable unit cell orientation for the activation of basal slip or extension twinning, instead requiring yielding through the activation of non-basal slip systems [38, 39]. Compression of the forged material along LD and TD did not display a significantly different YS compared to as-cast material due to both materials exhibiting extension twinning as a the primary yield mechanism. A more detailed examination of the quasi-static results can be found in our earlier work [40].

3.3 Cyclic stress strain properties

The plot of cyclic stress-strain (σ_c-$\Delta\varepsilon_t/2$) of AZ31B alloy where σ_c is the peak stress at midlife in tension/compression and $\Delta\varepsilon_t$ is the total strain range, is shown in Fig. 5. The corresponding quasi-static stress-strain plots are also included up to a total strain of 1.0% for reference. It is obvious that the alloy in both as-cast and forged conditions displayed remarkably higher hardening behavior during cyclic loading compared to quasi-static loading. The cyclic tests indicated that the as-cast alloy achieved a 0.2% offset cyclic YS of 109 MPa and 97 MPa in

tension (Fig. 5a) and compression (Fig. 5b), which is significantly higher than the values in quasi-static tension (56 MPa) and compression YS (74 MPa). Similarly, the forged alloy also exhibits a significant improvement in cyclic YS of 200 MPa and 112 MPa in tension and compression, respectively. The forged AZ31B demonstrated an 84 % increase in cyclic tensile YS and a 16 % increase in cyclic compression YS compared to the as-cast alloy (Table 3). The mechanisms responsible for the substantial increase in the cyclic tension curve of the forged material are discussed later.

3.4 Hysteresis loops and fatigue life

Fig. 6 depicts typical engineering stress–strain hysteresis loops of the first and half-life cycles for a total strain amplitude of 0.2% and 1.0% for the as-cast and forged AZ31B. It is seen in Fig. 6a that the slope during the first reversal (tension) is the same in both conditions and for both low and high strain amplitudes which indicates that forging did not alter the elastic modulus of the alloy. Also in Fig. 6a, the as-cast alloy exhibits a symmetric hysteresis loop at the lower strain amplitude (0.2%) whereas when the strain amplitude is increased to 1.0%, a slightly concave shape appears in the hysteresis loop, which is an indication of mild activity of a twinning-detwinning mechanism (Fig. 6b). In contrast, the forged material exhibits asymmetric stabilized hysteresis loops (Fig. 6c) for strain amplitudes higher than 0.4%, which are similar to those observed for rolled or extruded AZ31B Mg alloys [28, 41]. It is worth noting the serrations (stress drop and reloading to the plateau stress) observed in the hysteresis loops during the compressive reversal for the forged material (Fig. 6a), and a possible explanation for these serrations is discussed in section 4.1.

The evolution of hysteresis loops for the forged material at strain amplitudes of 0.4% and 1.0% is included in Fig. 7. At the lower strain amplitude (Fig. 7a), the second cycle hysteresis loop has an obvious asymmetric shape. By cycle 100, the loop evolves to be virtually symmetric and this symmetry is maintained up to the half-life (cycle 2400) of the test. A similar evolution of low amplitude hysteresis loops was observed by Roostaei et al. for extruded AM30 alloy [24]. In comparison to the low strain amplitude test, at the high amplitude (Fig. 7b), pronounced asymmetry is observed at the second cycle and this asymmetry is maintained throughout the test.

Optical microscopy was performed on post-failure specimens of the as-cast and forged alloys tested at both low and high strain amplitudes and the results are included in Fig. 8. Residual twins are observed in both the as-cast and forged AZ31B at higher strain amplitudes, but are absent at lower strain amplitudes. Twinning in the cast material is restricted to a few favorably oriented grains whereas it is far more prolific in the textured forged material. Additionally, at high strain amplitude (Fig. 8d) the forged material demonstrated several instances of cracks nucleating at twin boundaries (yellow arrows). A high magnification SEM image of such cracks is shown in Fig. 9 (red arrows). A discussion on the mechanism responsible for the formation of these cracks is included in the discussion section.

The number of cycles to failure, $N_{f,}$ against the imposed total strain amplitudes ($\Delta\varepsilon_t/2$) for the AZ31B alloy in as-cast and forged conditions is plotted in Fig. 10, along with some data available in literature for wrought AZ31 processed via extrusion [42] and rolling [43]. The as-cast alloy displayed lower fatigue life to that of the forged Mg alloy at high strain amplitudes and significantly shorter life compared to the forged alloy at low strain amplitudes. The other conditions (from literature) generally exhibited lower fatigue life for the same total strain amplitude. It should be noted that the fatigue life is always higher in forged material compared to the rolled and extruded materials above a total strain amplitude of 0.6%. The Coffin-Manson fatigue life parameters were evaluated and are listed in Table 4. It is also observed that the obtained Manson-Coffin parameters for the forged material in this study were considerably higher compared to the as-cast alloy and those obtained for wrought AZ31 obtained in other studies [43, 42].

3.5 Cyclic deformation response

Fig. 11 depicts the obtained stress amplitudes with respect to the number of cycles at several different total strain amplitudes on a semi-log scale. It is seen that the forged alloy always exhibited higher peak stress amplitude compared to the as-cast material for a particular strain amplitude (Fig. 11c). In order to characterize the cyclic hardening exhibited by the two material conditions, a power function of the form shown in Eq. (1) was fitted to the curves in Fig. 11a,b for cycles up to just prior to failure.

$$\sigma_a = AN^b \quad (1)$$

Where σ_a is the stress amplitude, N is the number of cycles, and A and b are the fitting parameters. The values of these fitting parameters along with their respective correlation coefficients are included in Table 5. The cyclic hardening rate $d\sigma_a/dN$ derived from Eq. (1) was then plotted for the as-cast and forged alloys for the first 10 cycles and is included in Fig. 11d. It is seen from this plot that at each cycle, the forged material demonstrates a higher cyclic hardening rate compared to the as-cast material for the same strain amplitude. Note that a more complex stress amplitude behavior was observed for the forged material at a low strain amplitude (0.2%). Specifically at this strain amplitude a certain extent of cyclic softening occurred up to ~80 cycles following which the material started to harden slightly until it reached the stabilization stage. Due to this behavior, a good fit to Eq. (1) was not obtained and this amplitude was therefore not included in Fig. 11d.

Additionally, during LCF testing, plastic strain amplitude is considered as a physical quantity that affects the microstructure and is strictly related to the resistance of strain. Thus plastic strain amplitude ultimately influences fatigue life. The obtained plastic strain amplitude ($\Delta\varepsilon_p/2$) during the current LCF tests is presented in Fig. 12, and the results correspond well with the change of the stress amplitude during cyclic loading as illustrated in Fig. 11 at different applied strain amplitudes. Note the considerable decrease in plastic strain amplitude in forged samples as the strain amplitude decreases.

3.6 Fatigue fracture surfaces

Fig. 13 shows SEM images of the as-cast and forged AZ31B alloy tested at two different total strain amplitudes of 0.3% and 1.0%. For the tested samples, three distinct features were observed on the fracture surface: (i) fatigue crack initiation (FCI), (ii) fatigue crack growth/propagation (FCG) zone and (iii) final fracture (FF) zone adjacent to the FCG zone. River like patterns with twin lamellae which are irregular or broken and grow along the crack propagation direction, were seen in all samples. However, profuse twin lamellae were observed in forged samples, especially at the higher strain amplitude of 1.0%. It is also noticed that multiple FCI sites (marked by red arrows) are visible in the samples tested at the higher strain amplitude (1.0%). At

the same time, at the higher strain amplitudes the fracture surfaces exhibit almost tensile-like fracture features for both as-cast (Fig. 13b) and forged specimens (Fig. 13d). Higher magnification images of the FCI areas are presented in Fig. 14 and show that most of the cracks initiated at the surface due to intrusion-extrusion (Fig. 14a) or casting defects such as large surface porosity (Fig. 14b) for the as-cast sample, and the presence of twin lamellae, secondary particles and oxide layers (Fig.14c, d) for the forged sample. These features act as stress concentrators which nucleate the fatigue cracks [30, 44]. The locations enclosed in green, white and yellow boxes in Fig. 13, are magnified and included in Fig. 15, Fig. 16 and Fig. 17, respectively to show more detailed features of the fatigue fracture surfaces corresponding to the as-cast and forged samples tested at total strain amplitude of 0.3% and 1.0%. As mentioned previously, the FCG zone is quite different depending on the alloy condition (i.e. cast versus forged). For example, the samples tested at a lower total strain amplitude (0.3%) exhibit fatigue striations (FS) within the FCG zone with each striation representing the growth of the crack during a load cycle. For this strain amplitude, the as-cast sample (Fig. 15a) revealed comparatively coarse FS with an average distance of 1.9 μm between striations, whereas, the forged sample (Fig. 15b) exhibited much finer FS (~ 0.5 μm between striations) surrounded by tear ridges. The finer FS observed in the forged specimens at lower strain amplitudes corresponds well with the considerably longer fatigue life observed in the forged material compared to the cast AZ31B (Fig. 10). Finally, the FF zone of the samples tested at a strain amplitude of 0.3% show ductile type fracture with dimples surrounded by tear ridges, with porosity in as-cast sample (Fig. 16a), and secondary cracks (marked by green arrows) in the forged sample (Fig. 16c). For tests at the high strain amplitude of 1.0% (Fig. 16b, d) typical ductile features (similar to those observed during quasi-static loading [40]) were observed all over the fracture surfaces. An interesting feature observed in the samples tested at all strain amplitudes is the presence of micro-cracks passing along or through intermetallics, which results in the generation of voids in the matrix (Fig. 17). With continued cycling, these voids coalescence leading to final fracture. Since the as-cast material contained a higher concentration of intermetallics compared to the forged sample (Fig. 2), more voids and cracks could be expected in the as-cast material contributing to the lower fatigue life.

4. Discussion

4.1 Deformation behavior

The mechanical properties of Mg alloys are strongly related to the crystallographic texture, which controls the slip and/or twinning system(s) activated during loading and thereby influences the tension-compression yield asymmetry [34, 45]. It is well established that $\{10\bar{1}2\}\langle 10\bar{1}1\rangle$ extension twinning and basal slip are the main room temperature deformation mechanisms in Mg alloys [30, 46]. As described in Section 3.1, the forged AZ31B developed a strong basal texture (Fig. 3) compared to the starting as-cast alloy. Additionally, the as-cast material contained precipitates of β-$Mg_{17}Al_{12}$ and $MgZn_2$ distributed along the inter-dendritic regions. The evolution of microstructure from the as-cast to the forged material includes the dissolution of precipitates and the recrystallization of grains (Fig. 2). Thus, forging at elevated temperature plays an important role in the formation of a strong basal texture which exhibits yield asymmetry of the forged AZ31B alloy (Fig. 4). As seen in Fig. 5 and Table 3, the ratio of the compression-to-tension cyclic yield stress was ~0.56 for forged material, compared to the as-cast material where the ratio was ~1. Additionally, the peak stress amplitudes of the forged alloy at all tested strain amplitudes were higher than the as-cast sample. This is an indication of improved fatigue strength in the forged material. The higher cyclic tensile curve of the forged alloy compared to the cast alloy is thought to be due to the contributions of: i) the overall strengthening of the forged alloy via grain refinement (Fig. 2) and hindrance of basal slip during tension due to the developed texture (Fig. 3), and ii) a pronounced twinning-detwinning mechanism resulting in extensive cyclic hardening. Twinning impacts the cyclic response of the current alloy which is generally governed by i) the cyclic stability of the microstructure, ii) gliding and multiplication of dislocations, iii) twinning-detwinning behavior, and iv) interactions between twins and dislocations. Particularly, strain hardening in the as-cast and forged materials was due to dislocation-dislocation interactions which impede their motion by interlocking. Profuse twinning in the forged material including higher residual twin density provides additional barriers to the movement of dislocations on the original slip plane leading to a pile-up of dislocations at the twin or grain boundary, which generates a back stress and thus contributes to additional strain hardening observed in Fig. 11 [47, 48].

It is also observed that compared to the as-cast material, the hysteresis loops of the forged AZ31B alloy (Fig. 6) were asymmetric. This asymmetry in the higher strain amplitude

hysteresis loops of the forged material is a result of twinning and subsequent detwinning during cyclic loading. At lower strain amplitudes (up to ~0.4%) in the forged material, extension twinning is activated during the initial compressive reversals due to the developed basal texture [49] and is evident by the shape of the second cycle hysteresis loop in Fig. 7a. During the following tensile reversal, detwinning occurs which is characterised by the early reverse yielding and a subsequent inflection due to the exhaustion of detwinning and activation of slip [50, 51, 52]. As the loading is repeated, cyclic hardening occurs in both tension and compression which appears to inhibit twin activation with continued loading. By the hundredth cycle (Fig. 7a), further extension twinning and corresponding detwinning appeared to be completely inhibited resulting in the development of a symmetric hysteresis loop. The symmetry of the hysteresis loop is retained up to the point of crack initiation. As the applied strain amplitude is increased, stresses during the compressive reversal are sufficient to activate more extensive extension twinning in favorably oriented grains. Detwinning occurs during the subsequent strain reversal however due to increasing dislocation density restricting dislocation motion, detwinning becomes difficult resulting in residual twins [15]. This phenomena is demonstrated in Fig. 7b where asymmetry is observed all the way up to the half-life (cycle 250) of the material. Similar twinning–detwinning behavior in wrought Mg alloys under cyclic loading were reported in [28, 50]. As pointed out in section 3.4, serrations were observed in the hysteresis loops during the compressive reversal for the forged material (Fig. 6a). These serrations are more pronounced during the initial reversals and normally disappear with continued cycling (Fig. 6c). This phenomenon was not observed under quasi-static compression, and is believed to be due to the different control modes (i.e., displacement control versus strain control), and accommodation of twin bands of localized deformation [53, 54].

An additional feature observed in the post-failure microstructure is the effect of intermetallics on twin growth. When the as-cast material is sufficiently loaded, twin bands originate and traverse the width of favorably oriented grains. However, intermetallics present within grains (Fig. 8b) act as barriers to these twins, inhibiting their growth, and limiting their influence on the overall deformation behavior of the alloy. Note that such intergranular intermetallics were only observed in the as-cast material (Fig. 2a). Instead, the post-failure forged microstructure displayed cracks along twin and grain boundaries (marked by arrows in Fig. 8 and Fig. 9). These cracks are

thought to be a result of dislocation buildup at twin boundaries. The underlying mechanism was reported by Hazeli et al. [55] during fatigue fracture of AZ31 Mg plate: i) At room temperature, extension twins may occur in a grain that have undergone profuse slip. These twins are formed as a result of a mechanism activated to accommodate the stain induced by slip. ii) Increasing the applied stress generates more dislocations, leading to the disassociation of the twin boundary which is related to magnitude of the imposed strain. iii) When the loading direction changes (i.e. after a reversal) twin boundary migration is reversed (i.e. detwinning occurs). However, as detwinning is a harder process requiring additional strain for completion, some residual twins remain in the fully reversed strain controlled fatigue test. iv) This twinning-detwinning mechanism is repeated during cycling leading to accumulation of dislocations at these residual twin boundaries. v) This dislocation accumulation at twin boundaries may then result in the nucleation of a fatigue crack along the twin boundary.

Fig. 10 demonstrated that the forged material exhibited longer fatigue life compared to the as-cast material particularly at lower strain amplitudes. This can be attributed to the difference in microstructural features present in the as-cast and forged conditions. Firstly, in both cast and forged materials, the crack originated at the specimen surface. This is due to higher propensity for unconstrained plastic flow to develop at a free surfaces resulting in surface roughening and eventually crack nucleation. In the case of the cast material, the crack initiation zone was found to contain intrusion-extrusion features and/or near surface voids (Fig. 14 a, b) which served as stress concentrators, thereby facilitating early crack formation [56]. In contrast, crack nucleation in the forged material may be a result of plastic strain accumulation at twin boundaries due to the buildup of non-reversible twins during cycling as was reported in [30, 55]. This is supported by the presence of numerous twin lamellae in the fatigue crack initiation region of the forged material (Fig. 14 c, d). Besides the mechanisms responsible for crack initiation, it is also well known that grain size plays an important role in controlling the crack growth rate with grain boundaries acting as barriers to the advancing crack front [57, 14]. Consequently, the relatively low grain boundary density in the as-cast alloy is thought to provide less impedance to crack propagation compared to the considerably higher grain boundary density observed in the recrystallized forged material. Further, other researchers have suggested additional roles for $\{10\bar{1}2\}$ extension twins (that were observed abundantly in the forged material) in lowering the

crack growth rate, for example, by extension twins serving as roughness induced crack closures [58, 59].

4.2 Fatigue modelling

Fatigue is the primary failure mechanism in most engineering components and therefore, accurate prediction of the fatigue life of an in-service component is of critical importance. In order to predict the fatigue damage per cycle and consequently the fatigue life of a material, several fatigue models that incorporate experimental fatigue life data have been proposed [60, 61, 62, 49]. The proposed models may be either stress-, strain- or energy-based however, as is visible in Fig. 6 and Fig. 10, lower stress does not necessarily imply longer fatigue life for the current alloy. Accordingly, a stress based approached may not be ideal for modelling the current alloy subjected to strain-controlled testing, although such an approach has been used for prediction of fatigue life under stress-control testing of AZ31B [63]. Additionally, the well-developed fatigue models currently available in literature were either established for isotropic materials, or developed for other forms of wrought Mg alloys (such as rolling or extrusions) with different characteristics than the current forged alloy. Consequently, the robustness of some available models to predict the fatigue life of the current forged AZ31B is investigated below.

During cyclic loading, total strain amplitude may be decomposed into elastic and plastic strain components [64, 65]:

$$\frac{\Delta\varepsilon_t}{2} = \frac{\Delta\varepsilon_e}{2} + \frac{\Delta\varepsilon_p}{2} \quad (2)$$

Where, $\frac{\Delta\varepsilon_t}{2}$ is the total strain amplitude, $\frac{\Delta\varepsilon_e}{2}$ is the elastic portion of the strain amplitude and $\frac{\Delta\varepsilon_p}{2}$ is the plastic portion of strain amplitude.

The relation between elastic strain amplitude and number of reversals fatigue life ($2N_f$) may be represented by the well-known Basquin equation [65, 66]:

$$\frac{\Delta\varepsilon_e}{2} = \frac{\sigma_f'}{E}\left(2N_f\right)^b \quad (3)$$

where E is Young's modulus, N_f is the number of cycles to failure, σ_f' is the fatigue strength coefficient and b is the fatigue strength exponent.

Similarly, the relation between plastic strain amplitude and the number of reversals to failure can be represented by the Coffin-Manson equation [65, 66]:

$$\frac{\Delta\varepsilon_p}{2} = \varepsilon_f'(2N_f)^c \quad (4)$$

where ε_f' is the fatigue ductility coefficient and c is the fatigue ductility exponent.

Combining Eqs. (2), (3) and (4), fatigue life can be estimated using the following relationship known as the Coffin-Manson relation [65]:

$$\frac{\Delta\varepsilon}{2} = \frac{\sigma_f'}{E}(2N_f)^b + \varepsilon_f'(2N_f)^c \quad (5)$$

Elastic strain amplitudes and plastic strain amplitudes plotted versus reversals to failure ($2N_f$) for as-cast AZ31B are included in Fig. 18 as an example and the calculated Coffin-Manson parameters are summarized in Table 4 along with values obtained from literature for other thermo-mechanically processed AZ31B [43, 42].

A drawback of the Coffin-Manson relation discussed above is its inability to account for mean stress effects, resulting in inaccurate prediction for asymmetric materials such as Mg [58]. Consequently other models were developed to account of the effect of mean stress on fatigue life.

4.2.1 Smith-Watson-Topper (SWT) model

SWT was developed as a modification to the Manson-Coffin relation to account for mean stress affect by considering an energy-like parameter evaluated at the plane of maximum axial strain. The SWT parameter is related to fatigue life as:

$$\sigma_{n,max}\frac{\Delta\varepsilon}{2} = \frac{\sigma_f'^2}{E}(2N_f)^{2b} + \sigma_f'\varepsilon_f'(2N_f)^{b+c} \quad (6)$$

Where $\Delta\varepsilon/2$ is the normal strain amplitude, $\sigma_{n,max}$ is the maximum normal stress on the maximum normal strain plane and E is the modulus of elasticity. The fatigue life predicted using the SWT model (Eq. 6) is plotted against the experimentally obtained fatigue life in Fig. 19. The

solid diagonal line represents a perfect match whereas the diagonal orange and black dashed lines represent factor of 1.5 and factor of 2 bounds respectively between the predicted and experimental life. From Fig. 19 it is seen that all the experimental data lies within the factor of 2 bounds for both as-cast and forged condition within the tested strain amplitudes indicating that the SWT model is suitable for modelling the current test data including the subject forged AZ31B.

4.2.2 Jahed-Varvani (JV) model

In addition to the SWT model discussed above, an energy based fatigue model was also considered in this study. Energy based models are commonly used particularly for asymmetric/anisotropic materials due to the invariant nature of strain energy density. The current paper considers an energy model proposed by Jahed and Varvani that predicts fatigue life using elastic and plastic energy relations [67]. The significance of this energy model is in evaluation of material's fatigue parameters. The fatigue parameters in the JV model are calculated from experimentally obtained total energy density vs. life curves. The total strain energy density, E, is related to number of reversals, $2N_f$, as:

$$E = E'_e\left(2N_f\right)^B + E'_f\left(2N_f\right)^C \tag{7}$$

E'_e, B, E'_f, C are energy-based fatigue properties obtained analogous to those in the Manson-Coffin relation and are determined in the same way. The values of these fatigue parameters calculated for the current study have been summarized in Table 6. E is the total strain energy density which is composed of the plastic energy density and the positive elastic energy density [68], where the plastic portion of the energy density is the area enclosed by the half-life hysteresis loop and the positive elastic portion is calculated by:

$$E_e^+ = \frac{\sigma_{max}^2}{2E} \tag{8}$$

Where σ_{max} is the tensile peak stress of the hysteresis loop.

The plot of predicted life versus experimentally observed fatigue life obtained from this model is included in Fig. 20 along with dashed diagonal lines that represent factor of 1.5 and factor of 2 bounds as was shown for the SWT model. The majority of data was found to be clustered quite tightly about the ideal prediction (solid line) within a factor of 1.5. The tight clustering of data points about the ideal model demonstrates the good predictive power of the JV model in the current study and it has also been reported to provide good multiaxial fatigue life prediction in the case of extruded AZ31B [45, 61].

5. Conclusions

Strain-controlled fatigue tests were performed on as-cast and cast followed by forged AZ31B Mg alloy in order to evaluate the effect of forging on the low cycle fatigue life of the alloy. From the above presented results, the following conclusions can be made.

- Dynamic recrystallization resulted in the occurrence of grain refinement in the forged alloy along with a development of a basal texture such that the basal planes were perpendicular to the forging direction.
- The as-cast condition displayed symmetric cyclic tension-compression deformation due to the random texture of the cast alloy whereas, the forged condition displayed substantial asymmetry due to the activation of $\{10\bar{1}2\}\langle 10\bar{1}1\rangle$ extension twinning in compression and subsequent detwinning followed by slip during tension.
- In general, the forged material displayed in overall improvement in low cycle fatigue life compared to the as-cast material attributed to the refined grain morphology, absence of casting defects, dissolution of intermetallics and texture modification.
- The strain-based SWT model and energy-based JV model both yielded good fatigue life prediction for both as-cast and forging conditions within the tested strain amplitudes.

Acknowledgements

The financial support of the Natural Sciences and Engineering Research Council of Canada (NSERC) through the Automotive Partnership Canada (APC) program under APCPJ 459269–13 grant with contributions from Multimatic Technical Centre, Ford Motor Company, and Centerline Windsor are acknowledged. The authors would also like to thank L. Blaga of CanmetMATERIALS for assistance with the forging trials and Dr. X. Su of Ford Motor Company for the cyclic tests that were performed at their facilities.

References

[1] EPA Office of Transportation and Air Quality, "EPA and NHTSA Set Standards to Reduce Greenhouse Gases and Improve Fuel Economy for Model Years 2017-2025 Cars and Light Trucks," United States Environmental Protection Agency, Washington, 2012.

[2] Q. Wang, B. Jiang, A. Tang, S. Ma, Z. Jiang, Y. Chai, B. Liu and F. Pan, "Ameliorating the mechanical properties of magnesium alloy: Role of texture," *Materials Science & Engineering A,* vol. 689, pp. 395-403, 2017.

[3] M. L. Olguín-González, D. Hernández-Silva, M. A. García-Bernal and V. M. Sauce-Range, "Hot deformation behavior o fhot-rolled AZ31 and AZ61 magnesium alloys," *Materials Science & Engineering A,* vol. 597, pp. 82-88, 2014.

[4] D. Hou, T. Liu, D. Shi, H. Chen and H. Chen, "Study of twinning behaviors of rolled AZ31 magnesium alloy by interrupted in situ compressive tests," *Materials Science & Engineering A,* vol. 653, pp. 108-114, 2016.

[5] S. B. Yi, C. H. Davies, H. G. Brokmeier, R. E. Bolmaro, K. U. Kainer and J. Homeyer, "Deformation and texture evolution in AZ31 magnesium alloy during uniaxial loading," *Acta Materialia,* vol. 54, no. 2, pp. 549-562, 2006.

[6] C. Bettles and M. Gibson, "Current wrought magnesium alloys: Strengths and weeknesses," *Journal of the Minerals, Metals and Materials Society,* vol. 57, pp. 46-49, 2005.

[7] O. Duygulu and S. R. Agnew, "The effect of temperature and strain rate on the tensile properties of textured magnesium alloy AZ31B sheet," *Magnesium Technology,* vol. 237, p. 242, 2003.

[8] P. Gao, S. Q. Zhu, X. H. An, S. Q. Xu, D. Ruan, C. Chen, H. G. Yan, S. P. Ringer and X. Z. Liao, "Effect of sample orientation and initial microstructures on the dynamic recrystallization of a Magnesium alloy," *Materials Science & Engineering A,* vol. 691, pp. 150-154, 2017.

[9] P. S. Roodposhti, A. Sarkar and K. L. Murty, "Microstructural development of high temperature deformed AZ31magnesium alloys," *Materials Science & Engineering A,* vol. 626, pp. 195-202, 2015.

[10] J. Koike, T. Kobayashi, T. Mukai, H. Watanabe, M. Suzuki, K. Maruyama and K. Higashi, "The activity of non-basal slip systems and dynamic recovery at room temperature in fine-grained AZ31B magnesium alloys," *Acta Materialia,* vol. 51, no. 7, pp. 2055-2065, 2003.

[11] M. Marya, L. G. Hector, R. Verma and W. Tong, "Microstructural effects of AZ31 magnesium alloy on its tensile deformation and failure behaviors," *Materials Science and Engineering: A,* vol. 418, pp. 341-356, 2006.

[12] H. Hu, Y. Ying, Z. Ou and X. Wang, "Comparisons of microstructures and texture and mechanical properties of magnesium alloy fabricated by compound extrusion and direct extrusion," *Materials Science & Engineering A,* vol. 695, pp. 360-366, 2017.

[13] R. Ma, Y. Zhao and Y. Wang, "Grain refinement and mechanical properties improvement of AZ31 Mg alloy sheet obtained by two - stage rolling," *Materials Science & Engineering A,* vol. 691, pp. 81-87, 2017.

[14] M. Tsushida, K. Shikada, H. Kitahara, S. Ando and H. Tonda, "Relationship between Fatigue Strength and Grain Size in AZ31 Magnesium Alloys," *Material Transactions,* vol. 49, no. 5, pp. 1157-1161, 2008.

[15] G. Huang, T. Han, F. Pan, H. Zhang and J. Li, "Improving low-cycle fatigue properties of rolled AZ31 magnesium alloys by pre-compression," *Material and Design,* vol. 58, pp. 439-

444, 2014.

[16] Q. Huo, Z. Xiao, X. Yang, D. Ando, Y. Sotou and J. Koike, "Enhanced fatigue properties of cast AZ80 Mg alloy processed by cyclic torsion and low-temperature annealing," *Materials Science & Engineering A,* vol. 696, pp. 52-59, 2017.

[17] J. Peng, Z. Zhang, Y. Li, W. Zhou and Y. Wu, "Twinning-induced dynamic recrystallization and micro-plastic mechanism during hot-rolling process of a magnesium alloy," *Materials Science & Engineering A,* vol. 699, pp. 99-105, 2017.

[18] L. Wang, G. Huang, T. Han, E. Mostaed, F. Pan and M. Vedani, "Effect of twinning and detwinning on the spring-back and shift of neutral layer in AZ31 magnesium alloy sheets during V-bend," *Materials and Design,* vol. 68, pp. 80-87, 2015.

[19] P. Molnár, A. Ostapovets and A. Jäger, "Reversible motion of twin boundaries in AZ31 alloy and new design of magnesium alloys as smart materials," *Materials and Design,* vol. 56, pp. 509-516, 2014.

[20] S. Kleiner and P. J. Uggowitzer, "Mechanical anisotropy of extruded Mg–6% Al–1% Zn alloy," *Materials Science and Engineering: A,* vol. 379, no. 1-2, pp. 258-263, 2004.

[21] A. Jain and S. R. Agnew, "Modeling the temperature dependent effect of twinning on the behavior of magnesium alloy AZ31B sheet," *Materials Science and Engineering: A,* vol. 462, no. 1-2, pp. 29-36, 2007.

[22] X. Yang, Z. Jl, H. Miura and T. Sakai, "Dynamic recrystallization and texture development during hot deformation of magnesium alloy AZ31," *Transactions of Nonferrous Metals Society of China,* vol. 19, no. 1, pp. 55-60, 2009.

[23] M. Matsuzuki and S. Horibe, "Analysis of fatigue damage process in magnesium alloy AZ31," *Materials Science and Engineering A,* vol. 504, pp. 169-174, 2009.

[24] A. A. Roostaei and H. Jahed, "Role of loading direction on cyclic behaviour characteristics of AM30 extrusion and its fatigue damage modelling," *Materials Science and Engineering: A,* vol. 670, pp. 26-40, 2016.

[25] H. T. Kang and T. Ostrom, "Mechanical behavior of cast and forged magnesium alloys cast and forged magnesium alloys," *Materials Science and Engineering A,* vol. 490, pp. 52-56, 2008.

[26] M. Huppmann, M. Lentz, K. Brömmelhoff and W. Reimers, "Fatigue properties of the hot extruded magnesium alloy AZ31," *Materials Science and Engineering: A,* vol. 527, pp. 5514-5521, 2010.

[27] M. Kamakura, K. Tokaji, H. Shibata and N. Bekkuq, "Improvement of Fatigue Strength Due to Grain Refinement in Magnesium Alloys," in *Fracture of Nano and Engineering Materials and Structures*, Greece, 2006, pp. 235-240.

[28] S. H. Park, S. G. Hong, B. H. Lee, W. Bang and C. S. Lee, "Low-cycle fatigue characteristics of rolled Mg–3Al–1Zn alloy," *International Journal of Fatigue,* vol. 32, pp. 1835-1842, 2010.

[29] L. Wu, S. R. Agnew, Y. Ren, D. W. Brown, B. Clausen, G. M. Stoica, H. R. Wenk and P. K. Liaw, "The effects of texture and extension twinning on the low-cycle fatigue behavior of a rolled magnesium alloy, AZ31B," *Materials Science and Engineering A,* vol. 527, pp. 7057-7067, 2010.

[30] F. Yang, S. M. Yin, S. X. Li and Z. F. Zhang, "Crack initiantion mechanism of extruded AZ31 magnesium alloy in the very high cycle fatigue regime," *Materials Science and Engineering: A,* vol. 491, no. 1-2, pp. 131-136, 2008.

[31] M. Lalpoor, J. S. Dzwonczyk, N. Hort and S. E. Offerman, "Nucleation mechanism of Mg17Al12-precipitates in binary Mg–7 wt.% Al alloy," *Journal of Alloys and Compounds,* vol. 577, p. 73–76, 2013.

[32] S. H. Park, J. H. Lee, B. G. Moon and B. S. You, "Tension–compression yield asymmetry in as-cast magnesium alloy," *Journal of Alloys and Compounds,* vol. 617, pp. 277-280, 2014.

[33] L. H. Song, B. L. Wu, L. Zhang, X. H. Du, Y. N. Wang, Y. D. Zhang and C. Esling, "Cyclic deformation behaviors of AZ31B magnesium alloy in two different asymmetric loading manners," *Materials Science & Engineering A,* vol. 689, pp. 134-141, 2017.

[34] C. H. Davies, S. Yi, J. Bohlen, K. U. Kainer and H. -G. Brokmeier, "Synchrotron Radiation Investigation of Twinning in Extruded Magnesium Alloy AZ31," *Materials Science Forum,* Vols. 495-497, pp. 1633-1638, 2005.

[35] S. R. Agnew, C. N. Tome, D. Brown, T. M. Holden and S. C. Vogel, "Study of slip mechanisms in a magnesium alloy by neutron diffraction and modeling," *Scripta*

Materialia, vol. 48, pp. 1003-1008, 2003.

[36] R. E. Reed-Hill and R. Abbaschian, Physical Metallurgy Principles, Third Edition ed., Boston: PWS-Kent Publishing Company, 1994.

[37] A. Gryguc, H. Jahed, B. Williams and J. McKinley, "MagForge – Mechanical Behaviour of Forged AZ31B Extruded Magnesium in Monotonic Compression," *Materials Science Forum,* Vols. 828-829, pp. 291-297, 2015.

[38] B. Q. Shi, R. S. Chen and W. Ke, "Effects of forging processing on the texture and tensile properties of ECAEed AZ80 magnesium alloy," *Materials Science and Engineering: A,* vol. 546, pp. 323-327, 2012.

[39] S. Seipp, M. F.-X. Wagner, K. Hockauf, I. Schneider, L. W. Meyer and M. Hockauf, "Microstructure, crystallographic texture and mechanical propertiesof the magnesium alloy AZ31B after different routes of thermo-mechanical processing," *International Journal of Plasticity,* vol. 35, pp. 155-166, 2012.

[40] D. Toscano, S. K. Shaha, B. Behravesh, H. Jahed and B. Williams, "Effect of Forging on Microstructure, Texture and Uniaxial Properties of Cast AZ31B Alloy," *Journal of Materials Engineering and Performance,* 2017.

[41] R. Zhu, X. Cai, Y. Wu, L. Liu, W. Ji and B. Hua, "Low-cycle fatigue behavior of extruded Mg–10Gd–2Y–0.5Zr alloys," *Materials and Design,* vol. 53, pp. 992-997, 2014.

[42] X. Z. Lin and D. L. Chen, "Strain controlled cyclic deformation behavior of an extruded magnesium alloy," *Materials Science and Engineering: A,* vol. 496, pp. 106-113, 2008.

[43] F. Lv, F. Yang, Q. Q. Duan, Y. S. Yang, S. D. Wu, S. X. Li and Z. F. Zhang, "Fatigue properties of rolled magnesium alloy (AZ31) sheet: Influence of specimen orientation," *International Journal of Fatigue,* vol. 33, p. 672–682, 2011.

[44] H. Mayer, M. Papakyriacou, B. Zettl and S. E. Stanz-Tschegg, "Influence of porosity on the fatigue limit of die cast magnesium and aluminium alloys," *International Journal of Fatigue,* vol. 25, pp. 245-256, 2003.

[45] J. Albinmousa, H. Jahed and S. Lambert, "Cyclic axial and cyclic torsional behaviour of extruded AZ31B magnesium alloy," *International Journal of Fatigue,* vol. 33, no. 11, pp. 1403-1416, 2011.

[46] A. Jäger, P. Lukáč, V. Gärtnerová, J. Haloda and M. Dopita, "Influence of annealing on the microstructure of commercial Mg alloy AZ31 after mechanical forming," *Materials Science and Engineering A,* vol. 432, pp. 20-25, 2006.

[47] X. Y. Lou, M. Li, R. K. Boger, S. R. Agnew and R. H. Wagoner, "Hardening evolution of AZ31B Mg sheet," *International Journal of Plasticity,* vol. 23, p. 44–86, 2007.

[48] H. Yu, Y. Xin, A. Chapuis, X. Huang, R. Xin and Q. Liu, "The different effects of twin boundary and grain boundary on reducing tension-compression yield asymmetry of Mg alloys," *Scientific Reports,* vol. 6, pp. 1-8, 2016.

[49] J. Dallmeier, O. Huber, H. Saage and K. Eigenfeld, "Uniaxial cyclic deformation and fatigue behavior of AM50 magnesium alloy sheet metals under symmetric and asymmetric loadings," *Materials and Design,* vol. 70, pp. 10-30, 2015.

[50] S. Hasegawa, Y. Tsuchida, H. Yano and M. Matsui, "Evaluation of low cycle fatigue life in AZ31 magnesium alloy," *International Journal of Fatigue,* vol. 29, pp. 1839-1845, 2007.

[51] S. M. Yin, H. J. Yang, S. X. Li, S. D. Wu and F. Yang, "Cyclic deformation behavior of as-extruded Mg–3%Al–1%Zn," *Scripta Materialia,* vol. 58, no. 9, pp. 751-754, 2008.

[52] L. Wu, A. Jain, D. W. Brown, G. M. Stoica, S. R. Agnew, B. Clausen, D. E. Fielden and P. K. Liaw, "Twinning–detwinning behavior during the strain-controlled low-cycle fatigue testing of a wrought magnesium alloy, ZK60A," *Acta Materialia,* vol. 56, no. 4, pp. 688-695, 2008.

[53] D. Brown, A. Jain, S. R. Agnew and B. Clausen, "Twinning and Detwinning during Cyclic Deformation of Mg Alloy AZ31B," *Materials Science Forum,* vol. 539, pp. 3407-3417, 2007.

[54] Q. Yu, J. Zhang, Y. Jiang and Q. Li, "An experimental study on cyclic deformation and fatigue of extruded ZK60 magnesium alloy," *International Journal of Fatigue,* vol. 36, no. 1, pp. 47-58, 2012.

[55] K. Hazeli, H. Askari, J. Cuadra, F. Streller, R. W. Carpick, H. M. Zbib and A. Kontsos, "Microstructure-sensitive investigation of magnesium alloy fatigue," *International Journal of Plasticity,* vol. 68, pp. 55-76, 2015.

[56] D. Hull, Fractorgraphy: Obesrving, Measuring and interpreting Fracture Surface

Topography, Cambridge University Press.

[57] S. Zheng, Q. Yu and Y. Jiang, "An experimental study of fatigue crack propagation in extruded AZ31B magnesium alloy," *International Journal of Fatigue,* vol. 47, pp. 174-183, 2013.

[58] Y. J. Wu, R. Zhu, J. T. Wang and W. Q. Ji, "Role of twinning and slip in cyclic deformation of extruded Mg–3%Al–1%Zn alloys," *Scripta Materialia,* vol. 63, pp. 1077-1080, 2010.

[59] S. Ando, Y. Ikejiri, N. Iida, M. Tsushida and H. Tonda, *J. Japan Inst. Metals,* vol. 70, pp. 634-637, 2006.

[60] K. N. Smith, T. H. Topper and P. Watson, "A stress-strain fuction for the fatigue of metals (stress-strain function for metal fatigue including mean stress effect)," *Jounral of Materials Science,* vol. 5, pp. 767-778, 1970.

[61] J. Albinmousa and H. Jahed, "Multiaxial effects on LCF behaviour and fatigue failure of AZ31B magnesium extrusion," *International Journal of Fatigue,* vol. 67, pp. 103-116, 2014.

[62] H. Jahed and J. Albinmousa, "Multiaxial behaviour of wrought magnesium alloys – A review and suitability of energy-based fatigue life model," *Theoretical and Applied Fracture Mechanics,* vol. 73, pp. 97-108, 2014.

[63] Y. C. Lin, Z.-H. Liu, X.-m. Chen and J. Chen, "Stress-based fatigue life prediction models for AZ31B magnesium alloy under single-step and multi-step asymmetric stress-controlled cyclic loadings," *Computational Materials Science,* vol. 73, pp. 128-138, 2013.

[64] K. L. Fan, G. Q. He, X. S. Liu, B. Liu, M. She, Y. L. Yuan, Y. Yang and Q. Lu, "Tensile and fatigue properties of gravity casting aluminum alloys for engine cylinder heads," *Materials Science and Engineering: A,* Vols. 78-85, p. 586, 2013.

[65] P. A. Rometsch and G. B. Schaffer, "An age hardening model for Al–7Si–Mg casting alloys," *Materials Science and Engineering: A,* vol. 325, pp. 424-434, 2002.

[66] S. K. Shaha, F. Czerwinski, W. Kasprzak, J. Friedman and D. L. Chen, "Monotonic and cyclic deformation behavior of the Al-Si-Cu-Mg cast alloy with micro-additions of Ti, V and Zr," *International Journal of Fatigue,* vol. 70, p. 383–394, 2015.

[67] H. Jahed and A. Varvani-Farahani, "Upper and lower fatigue life limits model using energy-

based fatigue properties," *International Journal of Fatigue,* vol. 28, pp. 467-473, 2006.

[68] K. Golos and F. Ellyin, "Generalization of cumulative damage criterion to multilevel cyclic loading," *Theoretical and Applied Fracture Mechanics,* vol. 7, no. 3, pp. 169-176, 1987.

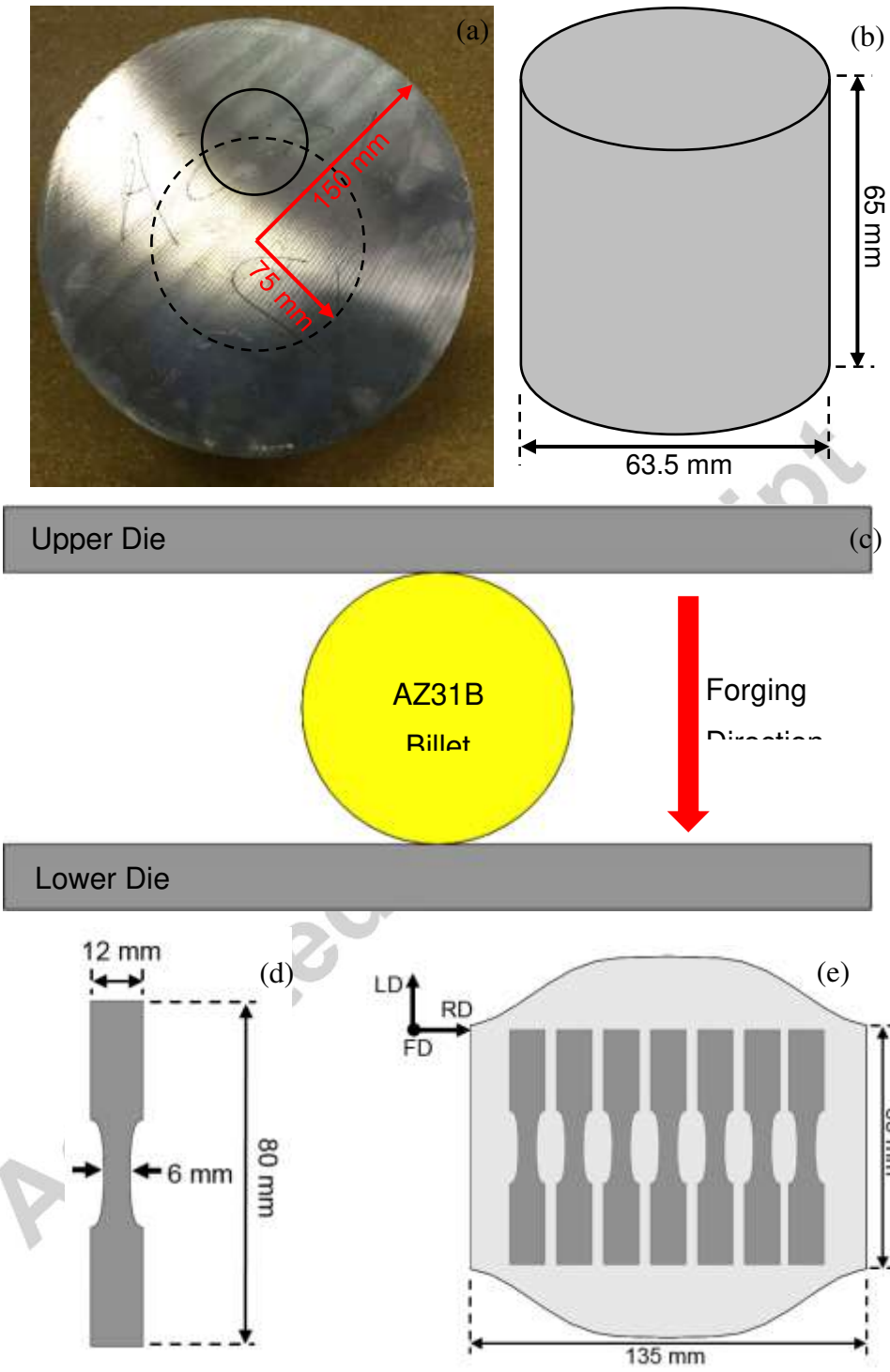

Fig. 1 Illustration of (a) the as-cast billet showing the extraction location (solid circle) for the smaller forged billet, (b) schematic of the smaller forged billet, (c) schematic of the forging process, (d) geometry of the dog-bone specimens and (e) dog-bone specimen extraction locations from the finished forging.

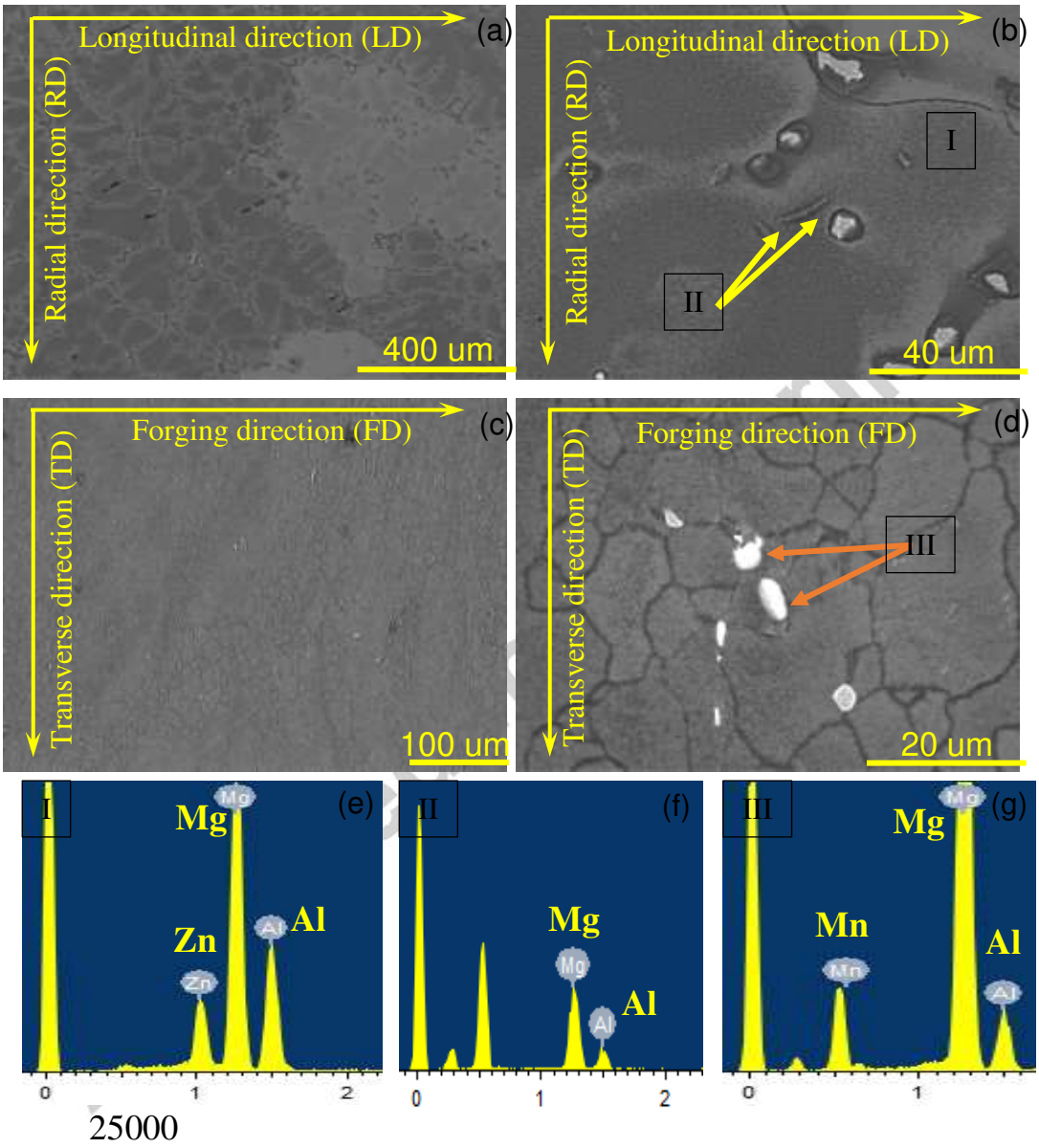

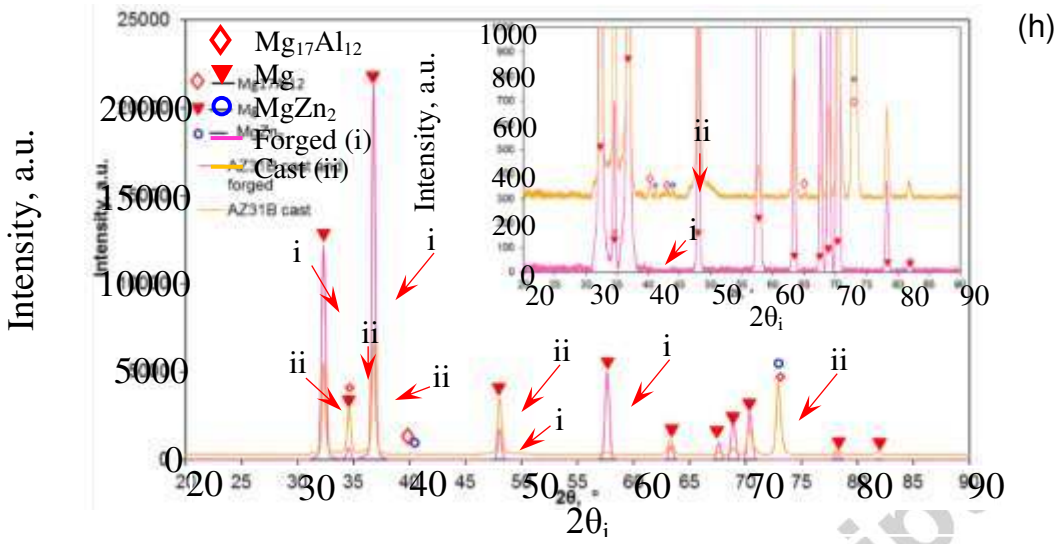

Fig. 2 SEM micrographs of AZ31B alloy in different conditions, (a, b) as-cast material and (c, d) cast followed by forged. EDX analysis of β-phase and Mg-Zn intermetallic is shown for the (e, f) as-cast sample at locations I and II respectively and (g) forged sample at location III. X-ray diffraction phase analysis of the (h) as-cast and forged material.

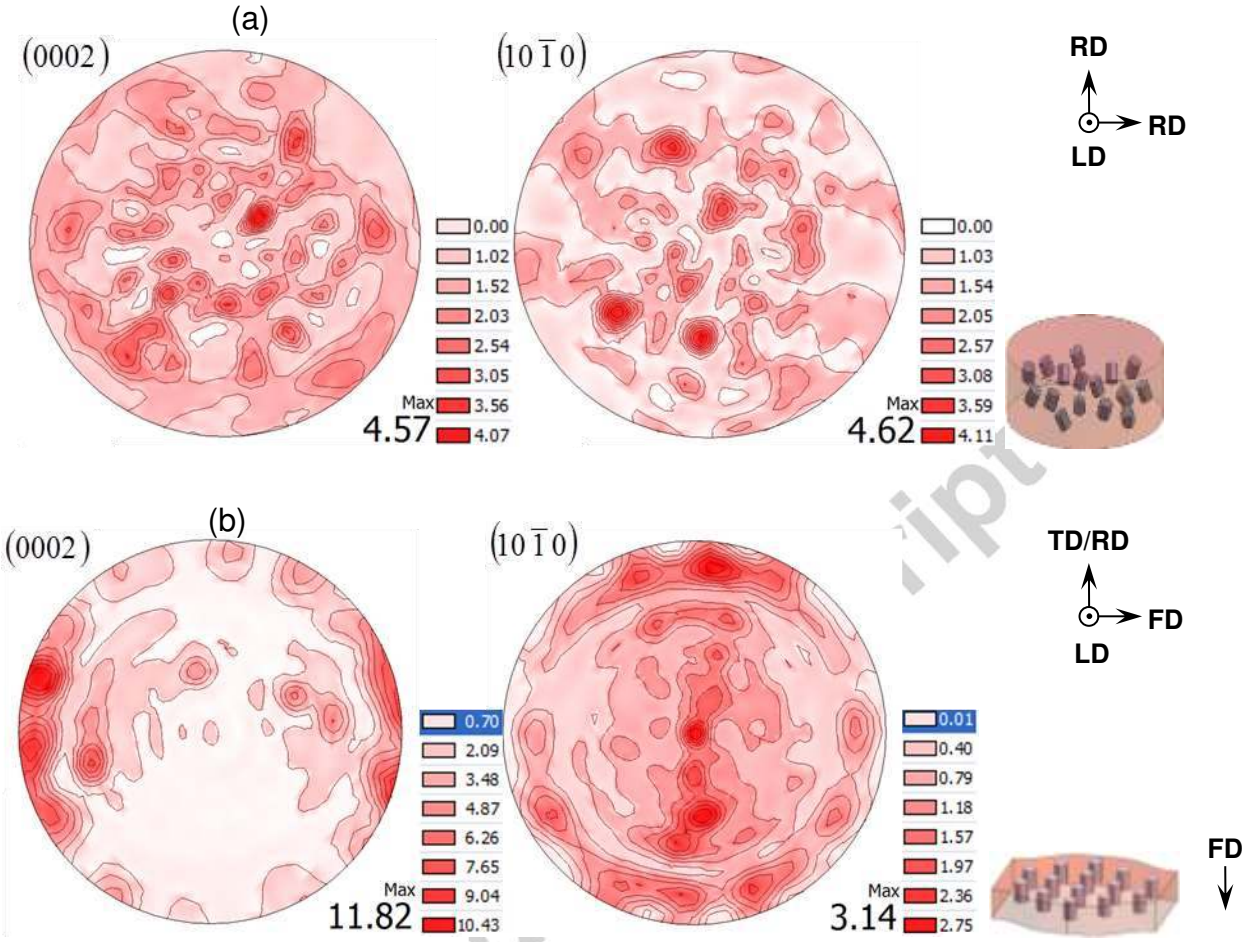

Fig. 3 Basal (0002) and prismatic $(10\bar{1}0)$ planes pole figures obtained for the AZ31B alloy samples (a) as-cast and (b) forged. Note: RD: Radial direction, LD: longitudinal direction, FD: forging direction, TD: Transverse direction.

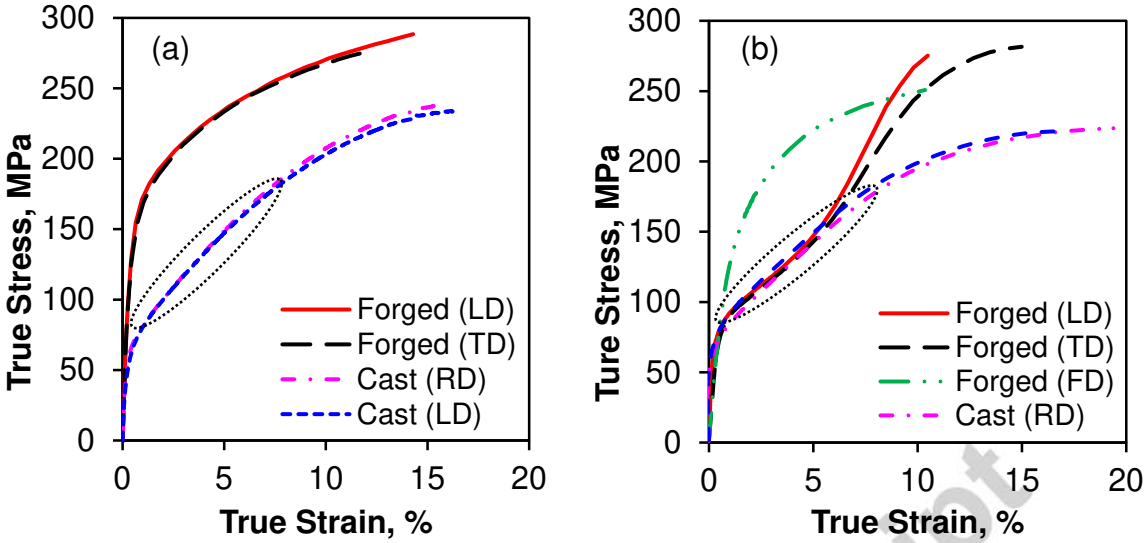

Fig. 4 Quasi-static behavior of as-cast and forged AZ31B tested in (a) tension and (b) compression.

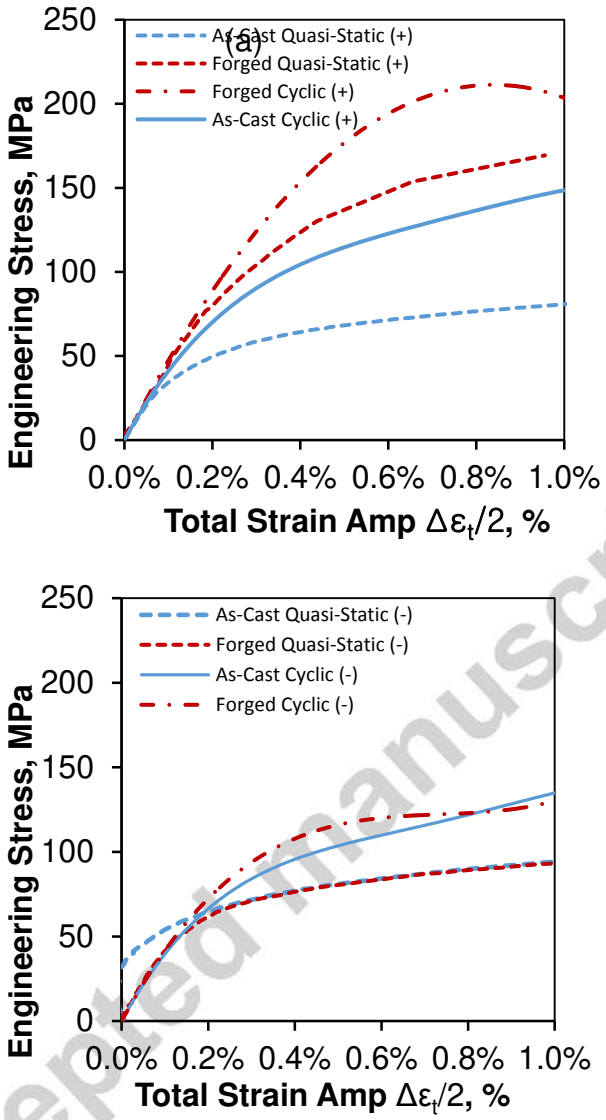

Fig. 5 Cyclic stress-strain curves derived from LCF test data showing (a) cyclic tension curves for cast and forged AZ31B and (b) cyclic compression curves for cast and forged AZ31B. For reference the related quasi-static curves have also been shown.

(a)

(b)

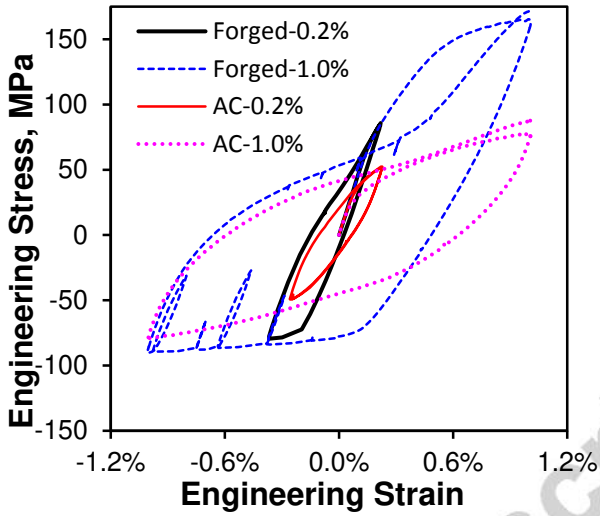

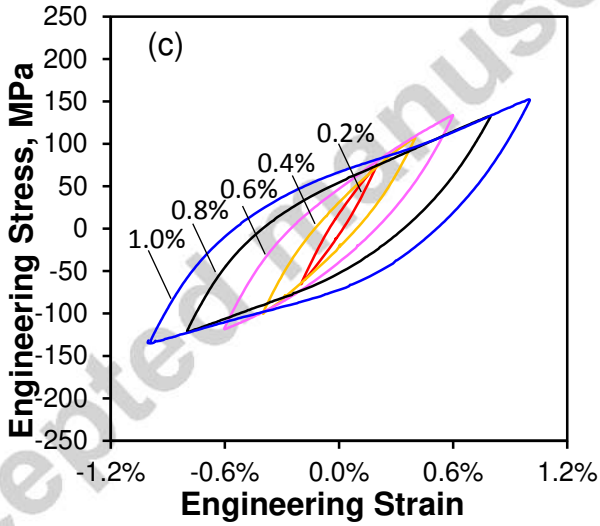

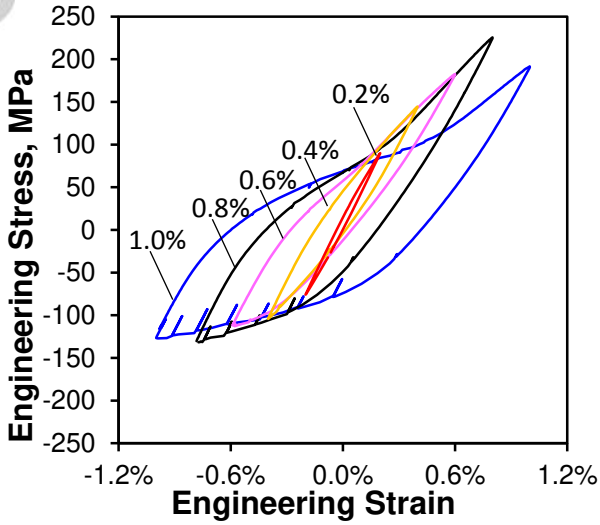

Fig. 6 Stress–strain hysteresis loops for (a) first cycle of the cast and forged materials and (b, c) half-life cycle for (b) as-cast and (c) forged AZ31B Mg alloy obtained from strain-controlled testing.

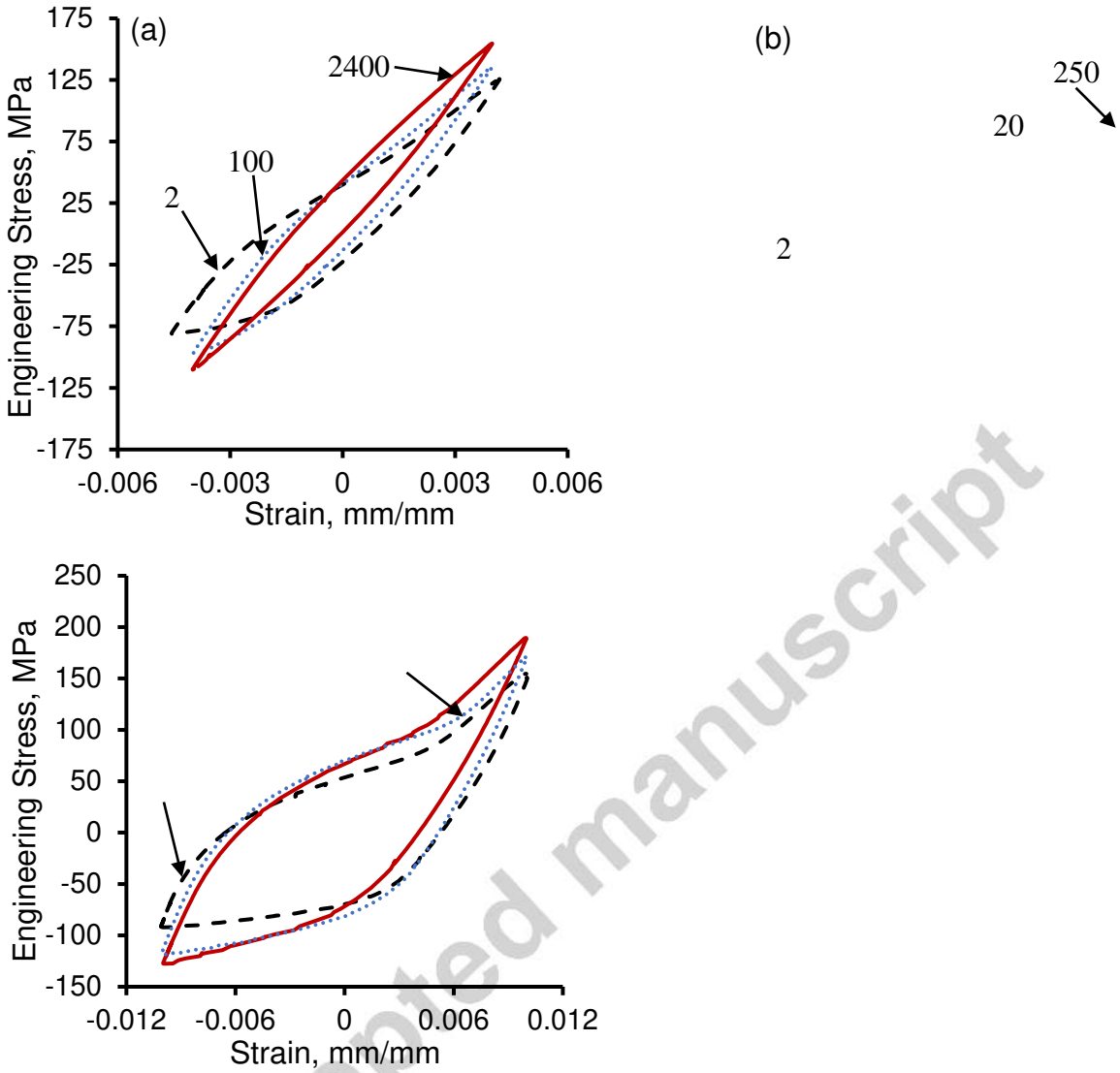

Fig. 7. Intermediate hysteresis loops for forged AZ31B tested at total strain amplitude of (a) 0.4% and (b) 1.0%. The 0.4% test failed after 4741 cycles whereas the 1.0% test failed after 497 cycles.

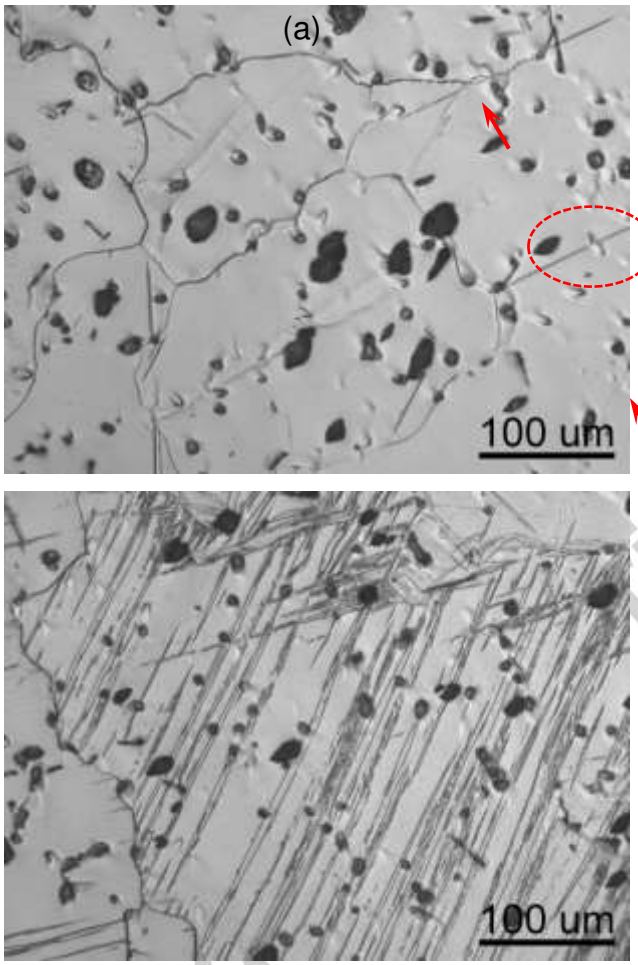

(b)

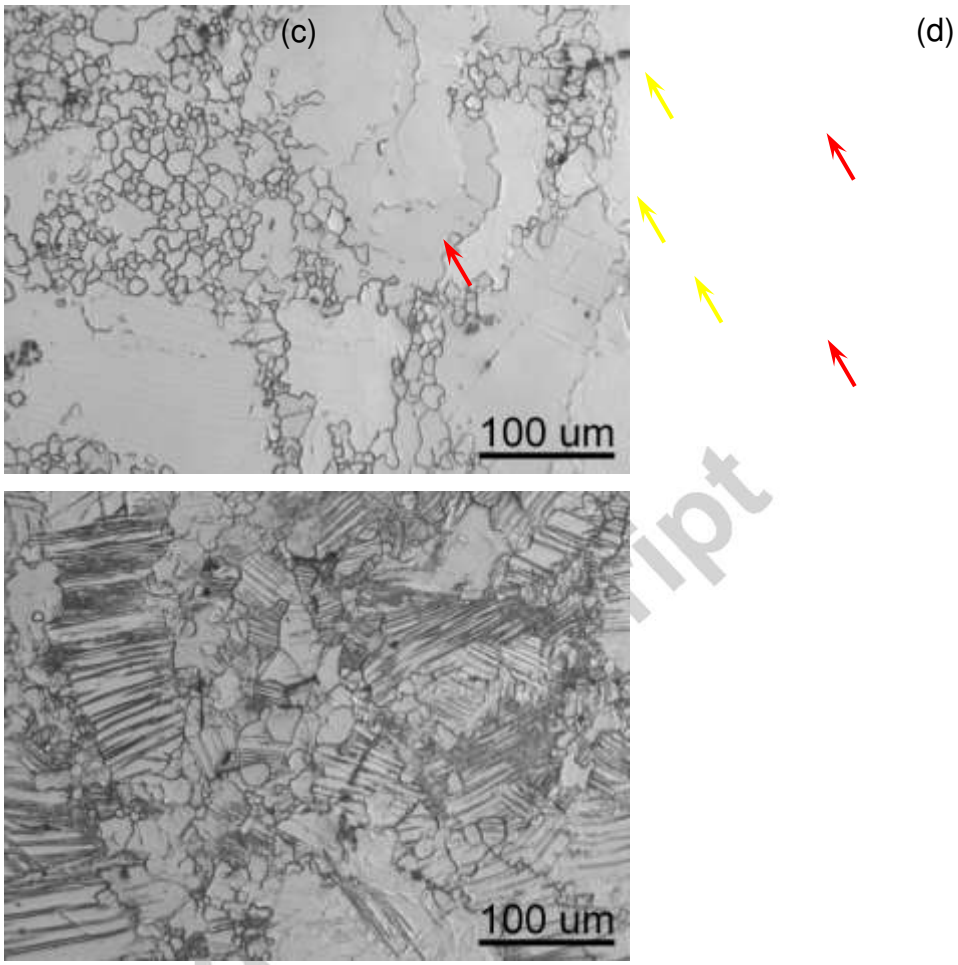

Fig. 8 Optical micrographs near the fracture surface at the gauge section of the (a, b) as-cast and (c, d) forged AZ31B Mg alloy observed post failure after testing at a total strain amplitude of (a, c) 0.3% and (b, d) 1.0%. The red and yellow arrows denote residual twins and cracks observed along twin boundaries respectively. The red ellipse denotes extension twins being blocked by intermetallics.

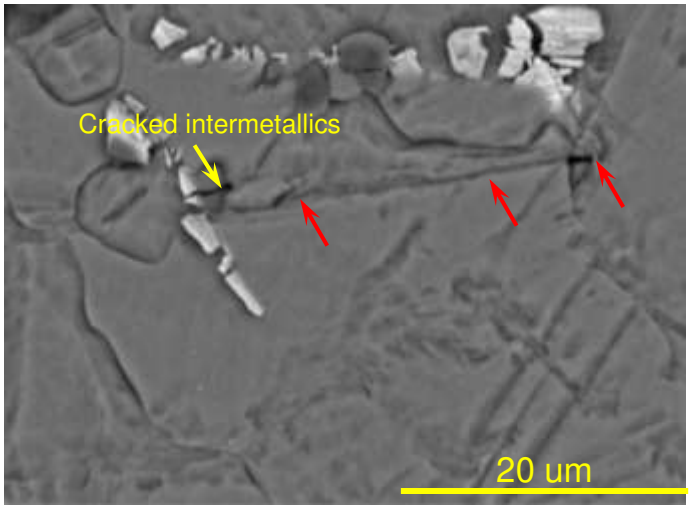

Fig. 9. SEM image of the polished gauge-section of forged material perpendicular to the fracture surface tested at a strain amplitude of 1.0%. Note the cracked intermetallics and secondary cracks (SC) along the twin boundary indicated by red arrows.

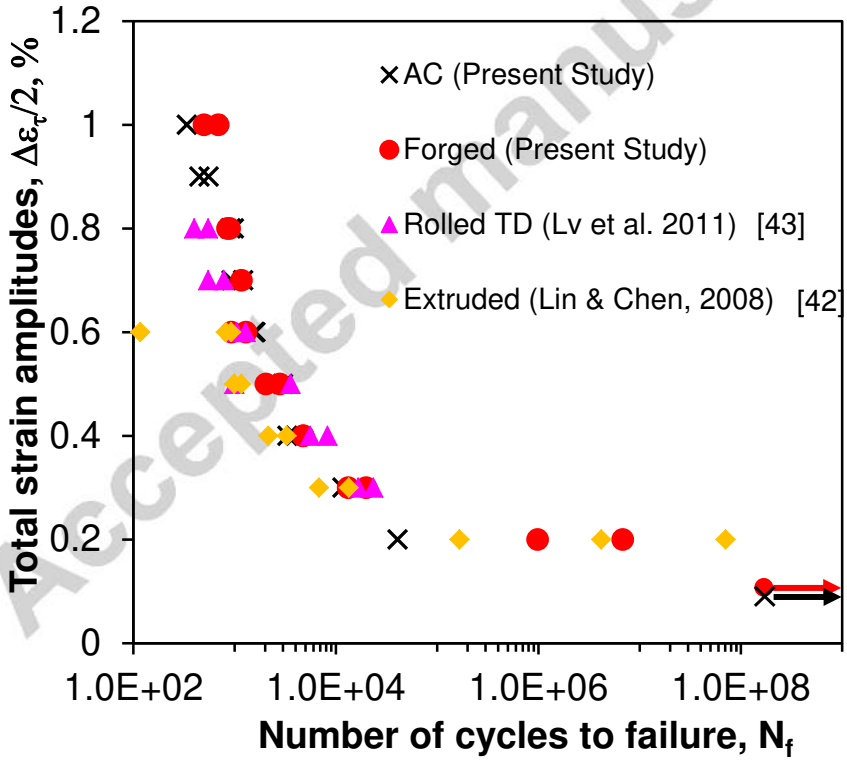

Fig. 10 Total strain amplitude vs. number of cycles to failure for cast and forged AZ31B Mg-alloy. Similar strain-controlled results for rolled and extrusion AZ31B Mg-alloy are presented for comparison.

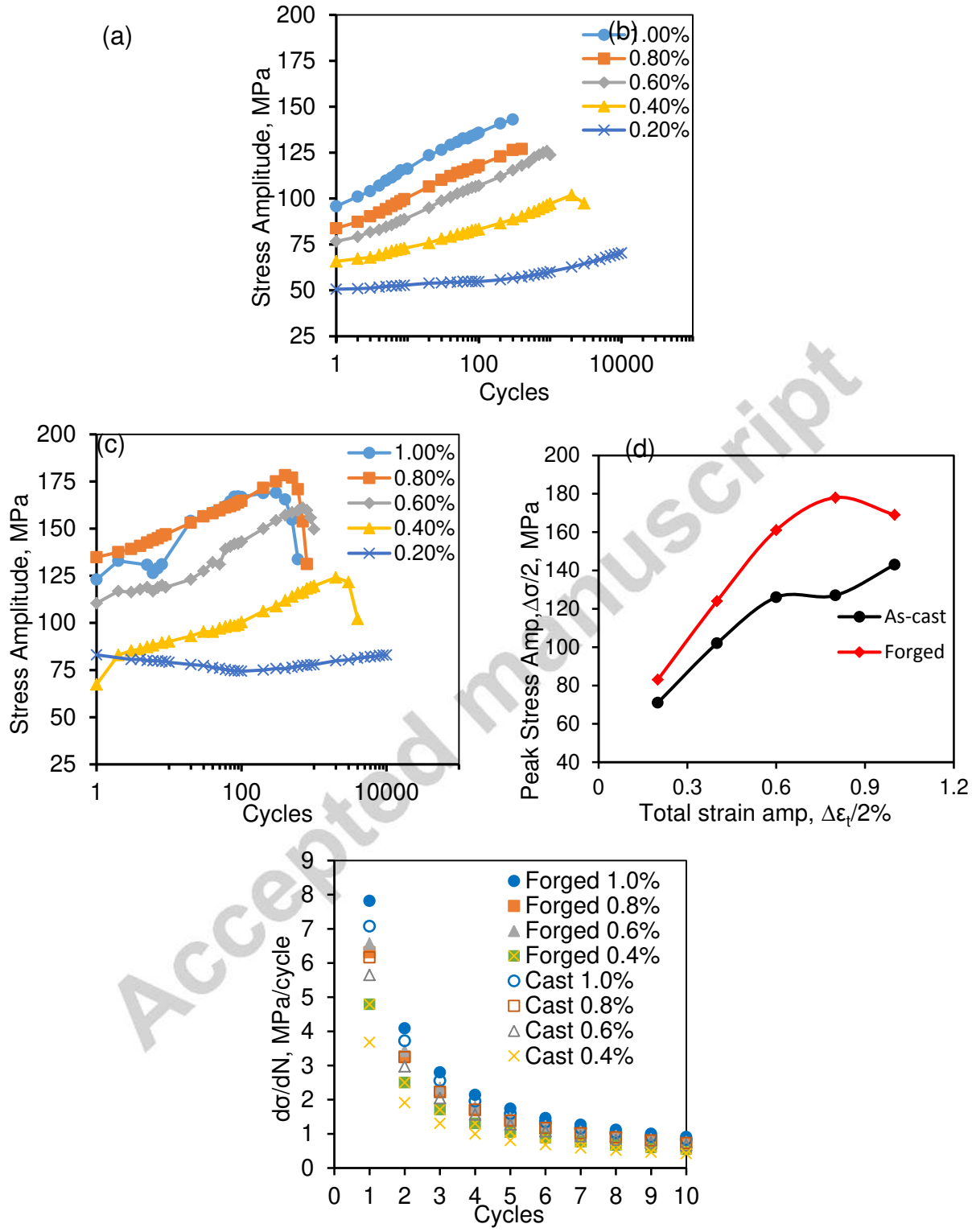

Fig. 11 Stress amplitude vs. number of cycles for AZ31B Mg alloy derived from LCF test data in (a) as-cast and (b) forged conditions, (c) a comparison of peak stress amplitude versus total strain

amplitude for the two material conditions and (d) plot of change in stress amplitude vs. cycles for cast and forged conditions.

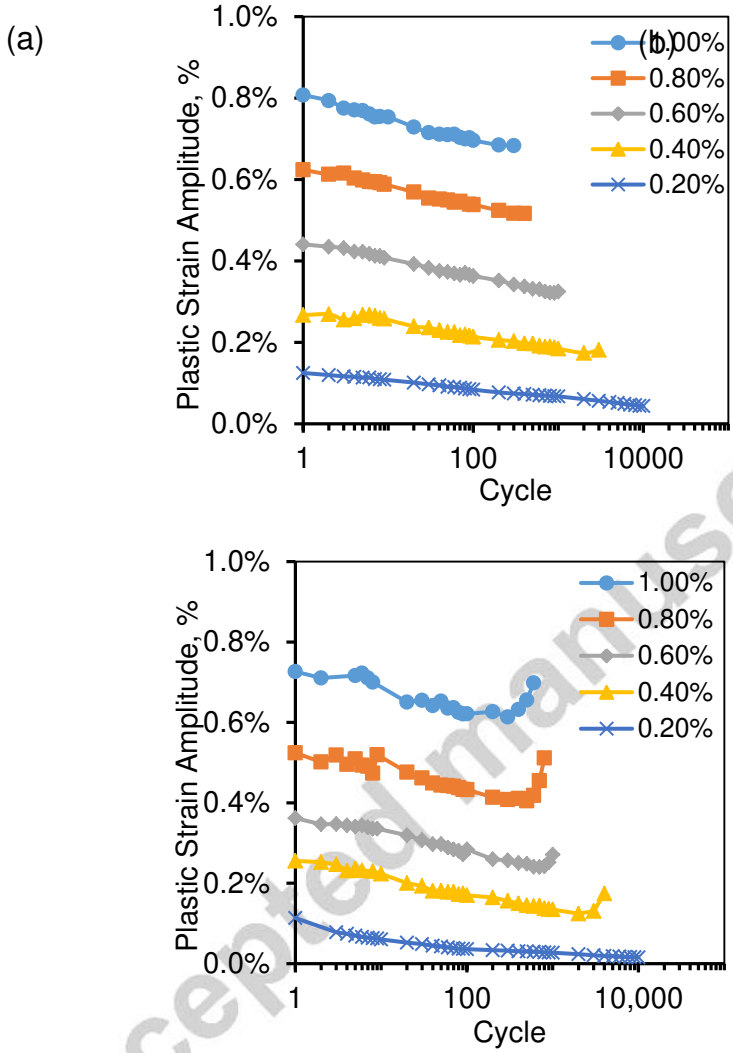

Fig. 12 Plastic strain amplitude vs. number of cycles for (a) as-cast and (b) forged AZ31B derived from LCF test data.

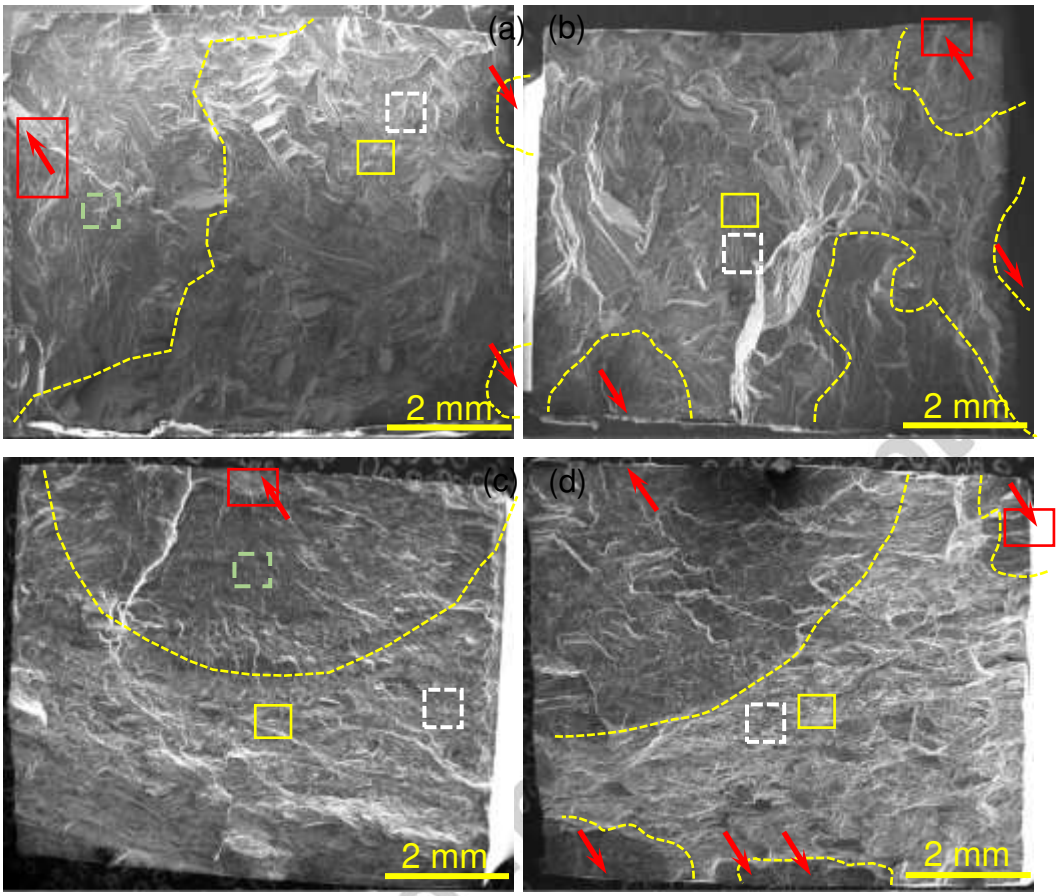

Fig. 13. SEM images of fatigue fracture surfaces of the samples tested at a total strain amplitude of 0.3% (a, c) and 1.0% (b, d) showing an overall view for as-cast (a, b) and forged (c, d) material. The yellow lines separate the fatigue crack growth (FCG) zone from the fast fracture (FF) zone. The red arrows indicate fatigue crack initiation (FCI). The enclosed boxes are magnified and presented in Fig. 14 (red boxes), Fig. 15 (green boxes), Fig. 16 (yellow boxes) and Fig. 17 (white boxes) showing the FCI, FCG, FF regions, and the presence of intermetallics, respectively, for the studied AZ31B Mg alloys.

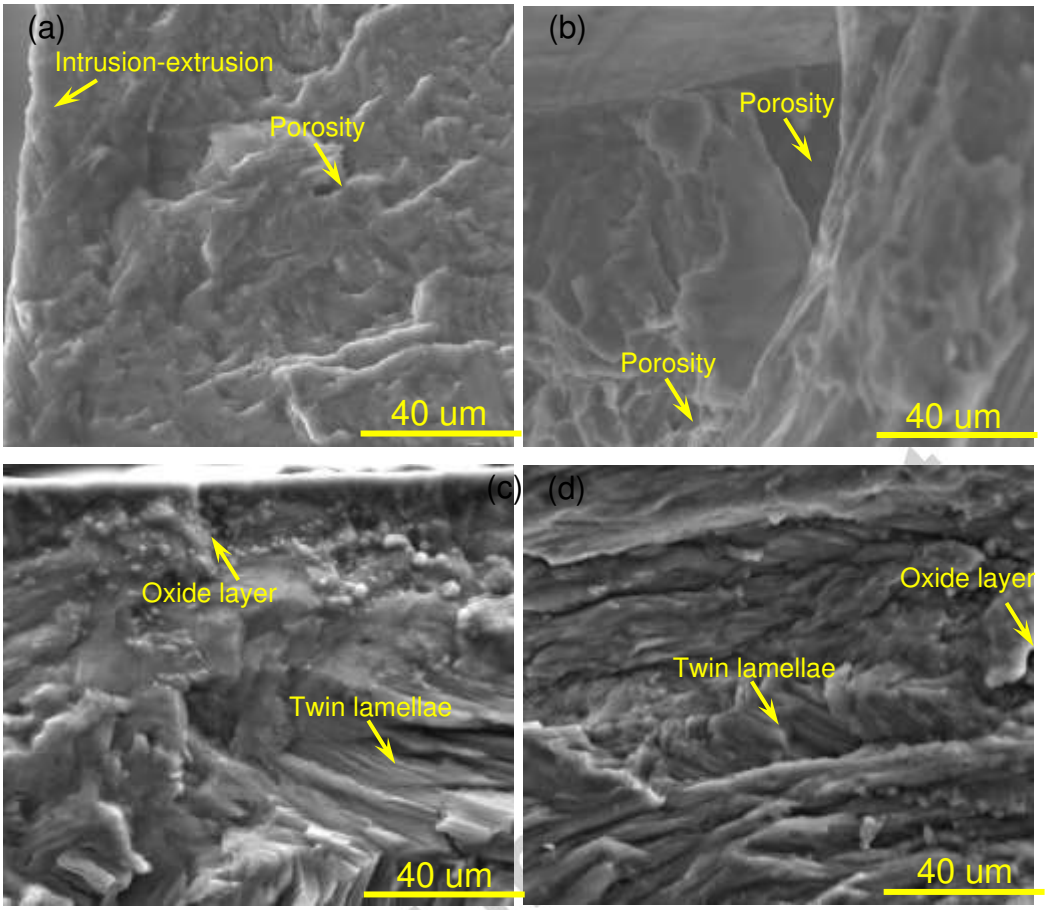

Fig. 14. SEM images of fatigue fracture surfaces of the samples tested at a total strain amplitude of 0.3% (a, c) and 1.0% (b, d) showing the crack initiation sites for as-cast (a, b) and forged (c, d). Note: fatigue cracks initiate due to (a) intrusion-extrusion, (b) the presence of a large surface pores, and (c, d) extension twin activity and oxide layers.

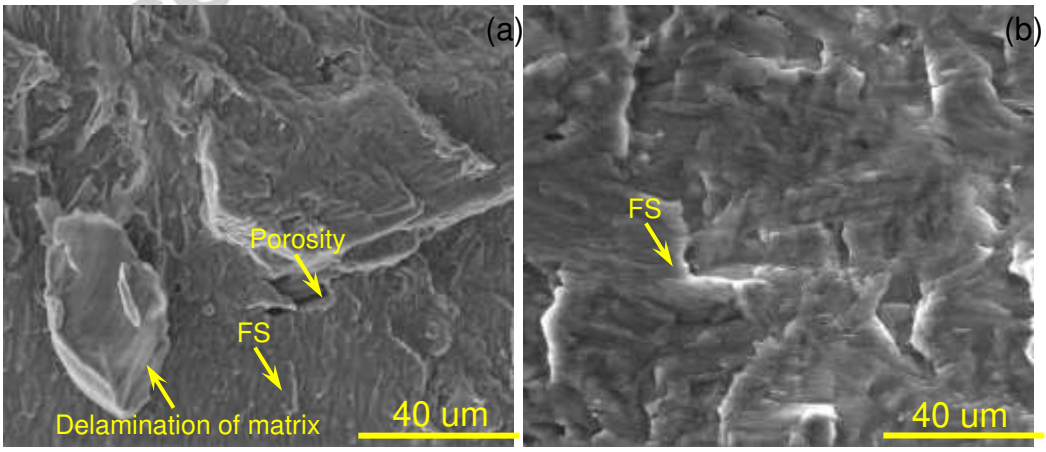

Fig. 15. SEM images of fatigue fracture surface in the FCG regions showing fatigue striation (FS) in the matrix of the samples tested at a total strain amplitude of 0.3% for (a) as-cast and (b) forged AZ31B.

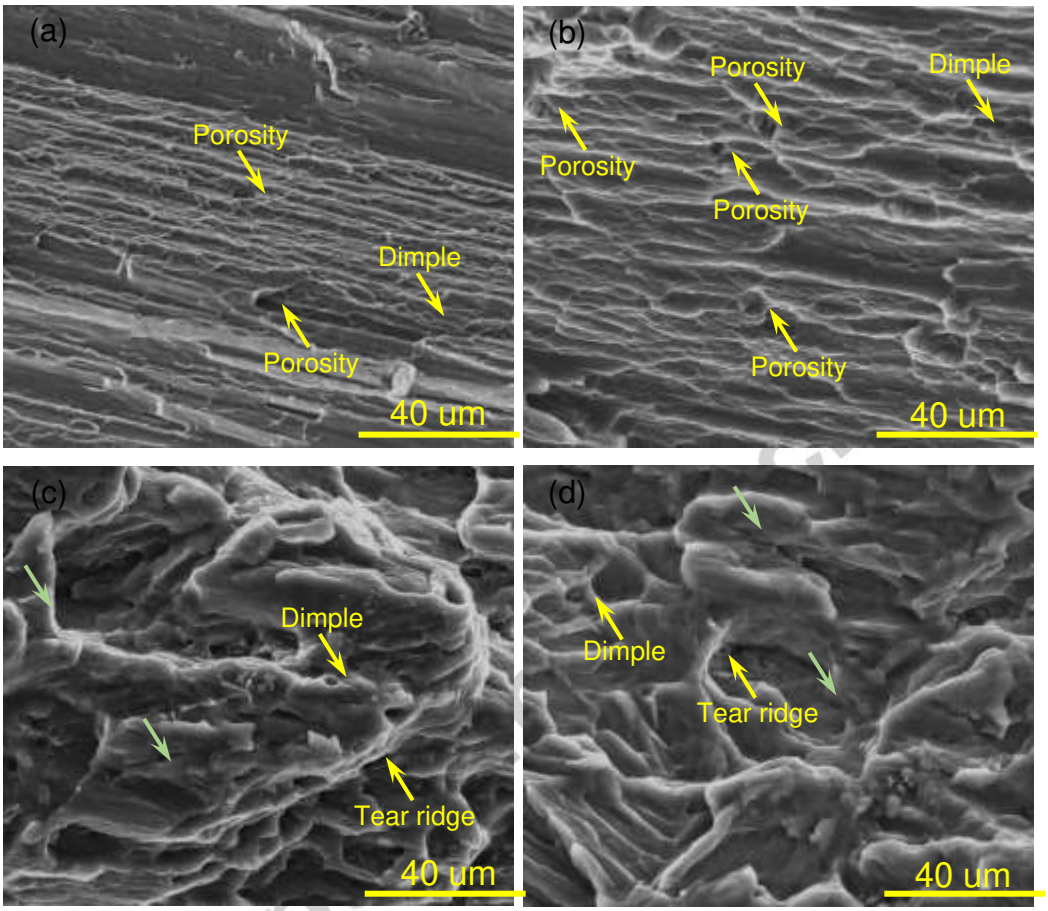

Fig. 16. SEM images of fatigue fracture surfaces of the samples tested at a total strain amplitude of 0.3% (a, c) and 1.0% (b, d) showing the morphology in the FF zone for the as-cast (a, b) and forged (c, d) AZ31B Mg alloy. Note: green arrows indicate the secondary cracks in the matrix.

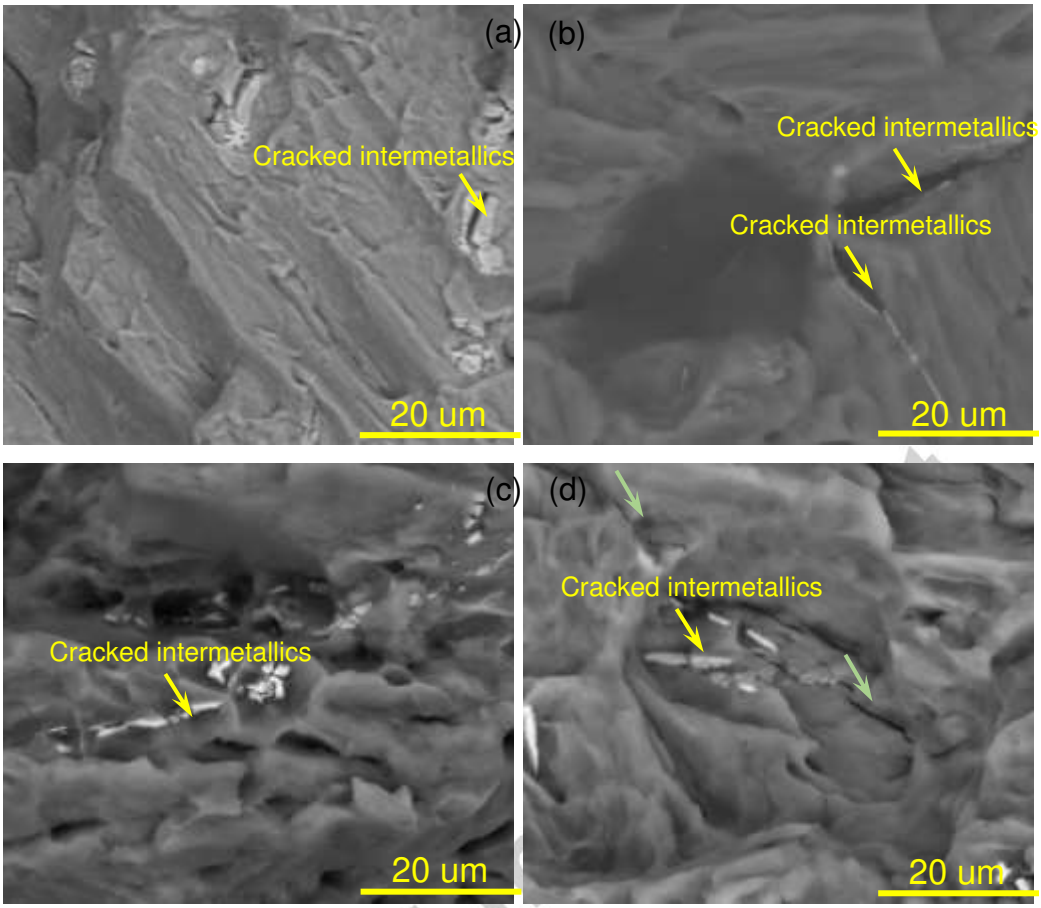

Fig. 17. SEM images of fatigue fracture surfaces of the samples tested at a total strain amplitude of 0.3% (a, c) and 1.0% (b, d) illustrating the role of intermetallics during cyclic loading of as-cast (a, b) and forged (c, d) material. Note: green arrows indicate the secondary cracks in the matrix.

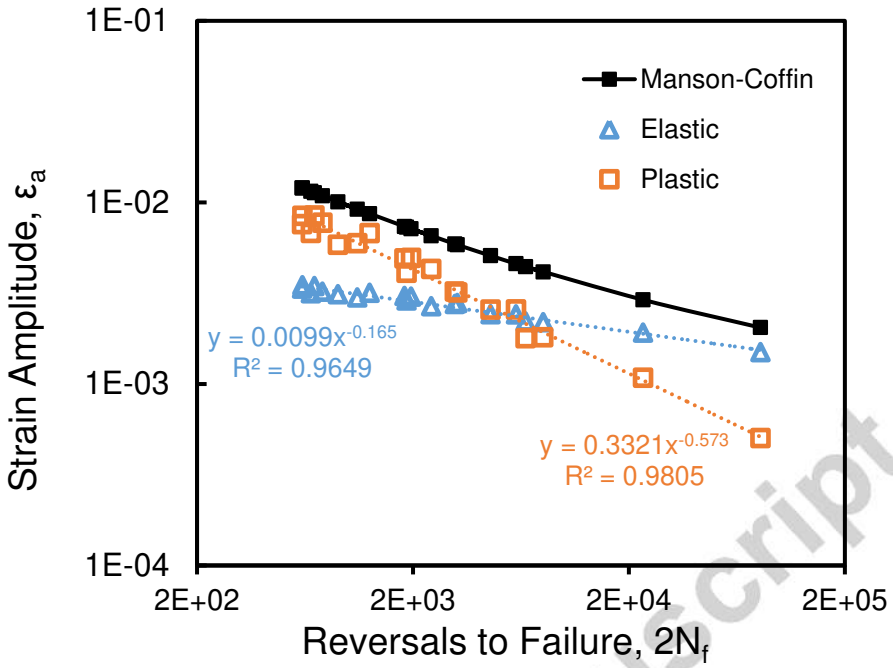

Fig. 18. Manson-Coffin plots for as-cast AZ31B LCF data on a logarithmic scale.

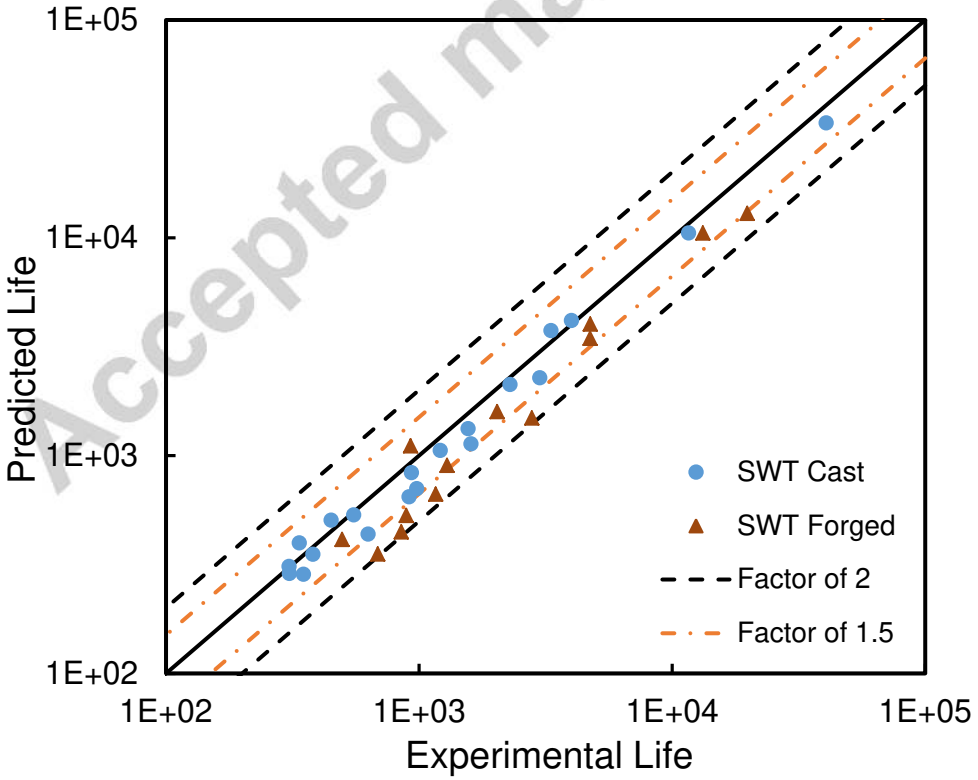

Fig. 19. Predicted fatigue life versus experimental fatigue life for as-cast and forged AZ31B using SWT fatigue model.

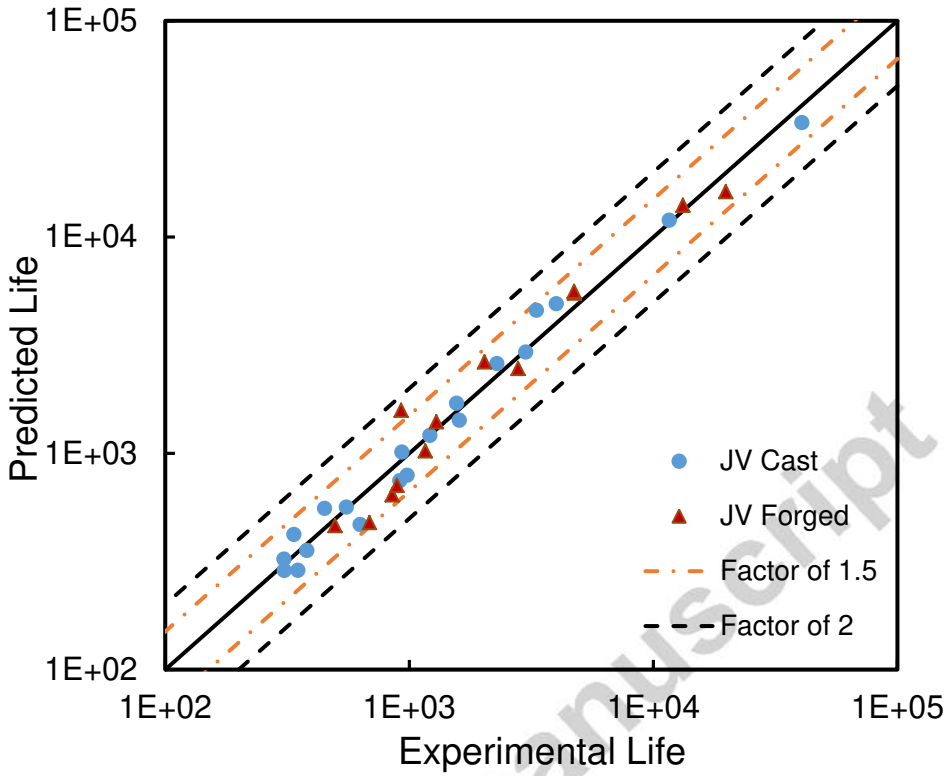

Fig. 20. Predicted fatigue life versus experimental fatigue life for as-cast and forged AZ31B using Jahed-Varvani fatigue model.

Table 1: Chemistry of AZ31B Mg-alloy in wt.%

Al	Zn	Mn	Cu	Cu	Ni	Fe	Ca	Others	Mg
2.99	0.95	0.2	0.05	0.05	0.005	0.005	0.04	0.3 in total	Bal

Table 2: Summary of monotonic tension and compression parameters of as-cast and forged AZ31B [Toscano et al. [40]].

		Tensile Properties			Compression Properties		
		YS, MPa	US, MPa	elong, %	YS, MPa	US, MPa	elong, %
Cast	LD/RD	56	235	15.7	74	268	18.8
Forged	LD/TD	136	278	12.4	78	316	13.2
	FD	-	-	-	116	278	10.4

Table 3: Summary of cyclic tension and compression yield stress for the tested as-cast and forged AZ31B alloy.

	Cyclic TYS, MPa	Cyclic CYS, MPa
Cast	109	97
Forged	200	112

Table 4: Summary of Manson-Coffin parameters for the tested as-cast and forged AZ31B alloy along with values found in literature for thermo-mechanically processed AZ31B.

	This Study		Lv et al., 2011[43]	Lin & Chen, 2008 [42]
Condition	Cast	Forged	Rolled	Extrusion
σ_f', MPa	396	482	434	467
b	-0.16	-0.14	-0.097	-0.13
ε_f', %	39	53	7.11	1.89
c	-0.59	-0.66	-0.49	-0.39

Table 5: Summary of curve fitting parameters and associated coefficient of determination for cyclic hardening behavior of as-cast and forged AZ31B.

	As-Cast			Forged		
Strain Amp.	A	b	R^2	A	b	R^2
1.0%	97.5	0.0726	0.987	121.2	0.064	0.865
0.8%	84.2	0.0732	0.991	132.6	0.048	0.996
0.6%	75.6	0.0747	0.997	107.1	0.061	0.969
0.4%	64.4	0.0572	0.991	76.6	0.062	0.952
0.2%	48.2	0.0354	0.912	-	-	-

Table 6: Summary of Jahed-Varvani energy parameters for the tested as-cast and forged AZ31B alloy.

	E'_e, MJ/m^3	B	E'_f, MJ/m^3	C
Cast	2.17	-0.319	387.5	-0.782
Forged	5.48	-0.332	344.6	-0.776